Leveraging geodetic GPS receivers for ionospheric scintillation science

Sebastijan Mrak[1], Joshua Semeter[1],Yukitoshi Nishimura[1],Fabiano S. Rodrigues[2], Anthea J. Coster[3], Keith Groves[4]

[1]Department of Electrical and Computer Engineering and Center for Space Physics, Boston University, Boston, MA, USA
[2]Center for Space Sciences, University of Texas at Dallas, Richardson, TX, USA
[3]Haystack Observatory, Massachusetts Institute of Technology, Westford, MA, USA
[4]Institute for Scientific Research, Boston College, Boston, MA, USA

Key Points:

- Scintillation analysis of 1 Hz geodetic receiver network cover 50 degree in latitude over the American longitude sector.
- Proxy scintillation indices are derived and validated.
- An event analysis reveal unprecedented storm-time scintillation evolution over North American continent.

Corresponding author: Sebastijan Mrak, `smrak@bu.edu`

Abstract

We demonstrate scintillation analysis from a network of geodetic Global Positioning System (GPS) receivers with 1 Hz data cadence. We introduce proxy phase (σ_{TEC}) and amplitude (SNR_4) scintillation indices, and validate them against rate of change of TEC index (ROTI), and S_4. Additionally, we validate scintillation observations against a CASES scintillation receiver. We develop receiver dependent scintillation event thresholding by virtue of hardware dependent noise variance. We analyze six-days adjacent to the 7-8 September 2017 geomagnetic storm, using 169 receivers covering magnetic latitudes between 15° and 65° in the American longitude sector. We leverage the available spatial sampling coverage to construct 2D maps of scintillation, and present episodic evolution of scintillation intensifications during the storm. We show that low-latitude and high-latitude scintillation morphology match well established scintillation climatology patterns. At mid-latitudes, spatiotemporal evolution of scintillation partially agrees with known scintillation patterns. Additionally, the results reveal previously undocumented mid-latitude scintillation producing structures. The results provide unprecedented view into spatiotemporal development of scintillation-producing plasma irregularities, and provide a resource to further exploit scintillation evolution at large spatial scales.

1 Introduction

The ionosphere significantly alters traversing radio signals at frequencies <3 GHz (ITUR-P.531-14, 2019), which include Global Navigation Satellite Systems (GNSS) signals. In particular, small-scale (<1 km) plasma density irregularities affect the L-band radio signals by means of Fresnel diffraction, causing the signal's amplitude and phase to rapidly fluctuate in a stochastic manner. A theoretical description of the diffracting scatter has been reviewed in detail (Yeh & Liu, 1982; Kintner et al., 2007; Priyadarshi, 2015). On the other hand, larger-scale plasma density irregularities (>1 km) impose fluctuations in received phase only, by means of signal refraction.

Extensive surveys of occurrence and climatology of both phase and amplitude scintillation have been conducted (Aarons, 1982; Basu et al., 1988; Wernik et al., 2003; Alfonsi et al., 2011; Jiao & Morton, 2015), primarily focusing on the low- and high-latitude regions. It has often been considered that necessary conditions for ionospheric density irregularities are confined to the equatorial and low-latitude regions (by Rayleigh-Taylor Instability), and high-latitudes (convection driven instabilities and particle precipitation). The mid-latitude ionosphere has not generally been perceived as a possible space weather threat for radio signal scintillation, with exceptions of equatorward expansion of high-latitude convection related dynamics (Kintner et al., 2007; Aarons, 1982). Despite the fact that significant amplitude scintillation was observed from the upstate New York during a geomagnetic storm (Ledvina et al., 2002), such scintillation occurrence geolocation and timing are not predicted by conventional scintillation models. For example, empirical scintillation models, wideband ionospheric scintillation model (WBMOD) (Secan et al., 1995, 1997) and the global ionospheric propagation model (GIM) (Béniguel, 2002), predict no signal impairments at mid-latitudes.

The historical surveys and existing models arise from insufficient availability of ground-based infrastructure for ionospheric scintillation monitoring. Many of the existing scintillation receivers are located at low- and high-latitudes, only a few scintillation receivers operate at mid-latitudes. Hence, a comprehensive analysis of ionospheric scintillation at mid-latitudes, by means of conventional amplitude (S_4) and phase (σ_ϕ), has been impossible. Generally, the scintillation receivers cover localized areas, hence the climatological statistics and occurrence timing is based on localized observations. We utilize 1-Hz GNSS receiver network operated by UNAVCO, which covers area from low- (15°MLAT) to high-latitudes (65°MLAT) over North America with data availability spanning back to 2011. Therefore the network analysis allows large spatial and instantaneous analy-

sis at unprecedented scales. The network consists of hundreds of receivers (∼200 in 2011, ∼850 in 2020), where the vast majority of the receivers monitor GPS signals only, thus we limit our study to the GPS.

Utilization of high-rate geodetic receivers is an attractive and potentially groundbreaking avenue for augmentation of GNSS scintillation science. Recently, several studies demonstrated capability of high-rate geodetic receivers on a single receiver comparison cases with co-located ionospheric scintillation monitors (Juan et al., 2017; Nguyen et al., 2019; Luo et al., 2020). The preliminary results were focused on the equatorial scintillation. Further Luo et al. (Luo et al., 2020) extended the capability to image amplitude scintillation over China. Contrary to the other studies, we make no attempt to calibrate the values of our scintillation indices to S_4 and σ_ϕ, since we have no co-located ionospheric scintillation monitors data available. We build upon the recent results, and present scintillation signal processing for a diverse receiver network, capable of imaging both, phase and amplitude scintillation, and monitoring instantaneous scintillation patterns over large spatial area. The purpose of this work is to promote utility of 1 Hz (hereafter referred as high-rate) geodetic receivers for scintillation science; specifically it is a diagnostic tool that provide unprecedented insight into small-scale dynamics of large-scale density features, such as storm time mid-latitude dynamics (Ledvina et al., 2002; Mrak et al., 2020).

We derive and validate alternative scintillation indices based on the signal-to-noise ratio (SNR), and total electron content (TEC). Despite the fact that each parameter is affected by different physical phenomenon (diffraction and refraction, respectively) (McCaffrey & Jayachandran, 2019), we make no attempt to distinguish among them. We introduce and validate receiver hardware-dependent thresholding for scintillation event decision. We demonstrate that the introduced indices are linearly correlated with S_4 and ROTI, respectively. Comparison with a CASES scintillation receiver from Dallas, TX, further support the validity of the introduced indices. The scintillation events are used to produce instantaneous scintillation maps. We demonstrate utility of the scintillation maps for spatiotemopral analysis of evolving scintillation. We analyze six days worth of data adjacent to 7-8 September 2017 geomagnetic storm. The low- and high-latitude portion of receiver network observed typical low- and high-latitude scintillation patterns. Additionally, the storm had a striking impact on the mid-latitude GPS receivers, exhibiting both amplitude and phase scintillation.

2 Methodology

We utilize publicly available data from the high-rate UNAVCO GPS receiver network, with available receiver distribution on 8 September 2017 depicted in Fig. 1. There is a heavy sampling bias toward the west coast of the continental United States (CONUS). Total distribution of receiver hardware types on that day is presented in Fig. 1b. The receiver network covers area between $15^\circ \leq$ magnetic latitude (MLAT) and $\leq 65^\circ$. Most of the receivers are placed within the contiguous US longitude span, whereas the high-latitude coverage comes from the Alaskan sector. In this study, we define mid-latitudes as the area between $30^\circ \leq \text{MLAT} \leq 60^\circ$ in the northern hemisphere.

Normally, scintillation studies use specialized GNSS scintillation receivers that provide amplitude (or power) and carrier phase at sub-second (usually 50 Hz) data-rate. These measurements are used to calculate σ_Φ, and S_4 scintillation indices. The high-rate geodetic receivers do not provide signal amplitude, and the carrier phase is contaminated by receiver imposed interference. We chose to utilize SNR provided by the Receiver Independent Exchange (RINEX) files, as a substitute for signal amplitude. SNR has inherently bigger variance than amplitude, as it is influenced by variance of a broadband noise. Additionally, SNR information provided by the RINEX files is by definition (computed) receiver dependent, and it is defined as a SNR of the demodulated carrier, namely carrier-

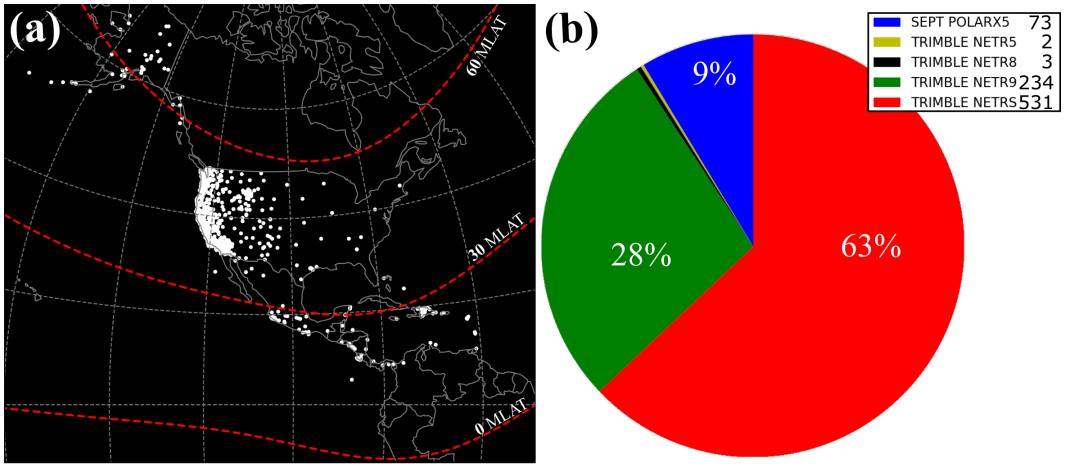

Figure 1. (a) Spatial distribution of available UNAVCO high-rate GPS receivers on 8 September 2017. (b) Receiver hardware type distribution on that day.

to-noise ratio. We build upon successful demonstrations of SNR utilization for scintillation studies (Thompson et al., 2008; Rodrigues & Moraes, 2019), and we evaluate behavior of scintillation indices for different receiver types.

We found an impediment with Trimble NETRS carrier phase measurements outlined in Fig. 2. The figure shows detrended L1CA (ΔL1) carrier phase converted to range measurements in panel (a). The 0.1 Hz high-pass filtered carrier phase δL1 in panel (b) shows numerous abrupt jumps in the carrier phase. The consequence of this impairment is that we can't use conventional phase scintillation index σ_Φ as it is defined on L1 carrier phase measurements. A peculiar nature of carrier phase, and its use for scintillation studies has been discussed by Beach 2006 (Beach, 2006). A carrier phase combination of L2P and L1CA channels in bottom two panels show the abrupt changes cancel out. The resulting detrended phase combination Δ(L2P-L1CA) in panel (c), and its high-pass filtered derivative show receiver hardware independent carrier phase perturbations, which can be used for extracting ionosphere scintillation effects. Trimble NETRS receivers comprise more than half of the UNAVCO receiver network, and thus we adopt the use of carrier phase combination instead of the L1 carrier phase throughout the network. As we show in the next section, carrier phase combination is proportional to the total electron content, and thus we utilize this property and the TEC as a measure of phase fluctuations. As suggested by Beach 2006 (Beach, 2006), the use of a TEC, that is, a weighted carrier phase combination, can eliminate the receiver imposed errors to phase measurements.

Measurements sampled at 1 Hz tend to undersample scintillations as the scintillation spectra extend to sub-second time scales. Carrier phase is not an issue as the power law dependence shall continuously extend into larger spatial scale (slower time scale at the receiver). It has been demonstrated that a 1 Hz receiver and a co-located scintillation receiver measure morphologically the same scintillation spectra above 0.5 Hz (Béniguel et al., 2009). On the other hand, amplitude scintillation spectra has a low frequency cut-off (phase screen approximation) at the Fresnel scale r_F ($r_F = \sqrt{2\lambda Z}$, Z being the distance between receiver and irregularity) (Kintner et al., 2007), which translates into Fresnel frequency $f_F = r_F\ v_0$, where v_0 is the irregularity drift. Thus, a 1 Hz receiver with a Nyquist frequency at 0.5 Hz, oversamples only scintillation producing irregularities with effective drift velocity $v_0 \leq$180 m/s (Rino, 1979). This calculation assumes isotropic irregularities at $Z = 350\ km$, with v_0 perpendicular to the line-of-sight.

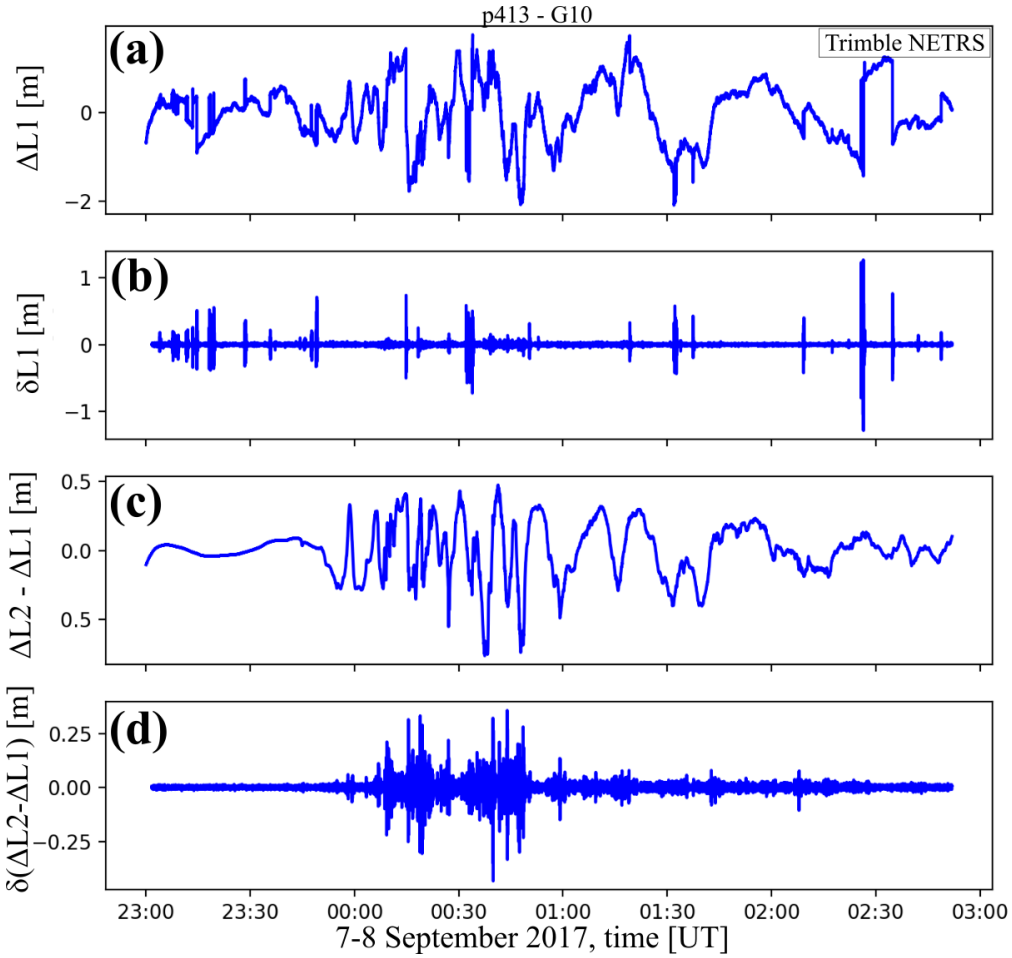

Figure 2. Carrier phase measurements (converted to range units) by the p413 receiver, measuring satellite G10, on 8 September 2017. (a) L1C detrended carrier phase. (b) High passed filtered (0.1 Hz) L1C carrier phase. (c) Differential carrier code measurements L2P-L1CA. (d) High-pass filtered differential carrier phase of L2P-L1CA.

2.1 Data processing

We utilize GPS data from RINEX files where we take SNR at L1 (f_1=1575.42 MHz), and deduct slant TEC (sTEC) from carrier phases L1CA and L2P (f_2=1227.6 MHz) expressed as ranges

$$sTEC = \frac{1}{40.3}\frac{f_1^2 f_2^2}{f_1^2 - f_2^2}(L_2 - L_1)10^{-16}\ [TECu], \tag{1}$$

where the carrier phase ambiguities and cycle slips are accounted for with a method of Blewitt et al.(Blewitt, 1990), and 1 TECu=10^{16}electrons per meter squared. The sTEC is derived from the phase accumulation property that the phase advance is inversely proportional to f^2 and proportional to $sTEC$ (δL=$\frac{40.3}{f^2}$ δsTEC) (Mrak et al., 2018). The sTEC is then converted to vertical (hereafter referred as TEC) assuming the thin shell ionosphere approximation via mapping function F(Θ) (?, ?)

$$F(\Theta) = \sqrt{1 - \cos^2(\Theta)\left(\frac{R_e}{R_e + h_{IPP}}\right)^2} \tag{2}$$

via zero TEC method (Rideout & Coster, 2006). Here, we assume the height of ionospheric piercing point (h_{IPP}) to be 350 km, R_e is the radius of the Earth, and Θ is the elevation angle. We apply a (6^{th}order) high-pass filter, with 0.1 Hz cutoff frequency and Butterworth response (Fremouw et al., 1978) to the sTEC and SNR, obtaining δTEC and δSNR, respectively. Scintillation indices σ_{TEC} and SNR_4 are then computed with a running 60-seconds standard deviation filter, normally used to compute phase scintillation index σ_ϕ.

$$\sigma_{TEC} = \sqrt{< \delta TEC^2 > - < \delta TEC >^2} \tag{3}$$

$$SNR'_4 = \sqrt{< \delta SNR^2 > - < \delta SNR >^2} \tag{4}$$

We further adjust low elevation measurements due to oblique angle propagation through irregularity layer using the approach by (Spogli et al., 2009; Alfonsi et al., 2011). Then SNR_4 can be expressed as:

$$SNR_4 = SNR'_4 \cdot F(\Theta)^{0.9} \tag{5}$$

Due to the problem with the carrier phase mentioned above, we compare the phase scintillation index σ_{TEC} against the rate of change of TEC (ROT) index (ROTI). We compute ROTI, utilizing a running 60-second standard deviation filter, as defined by (Pi et al., 1997),

$$ROTI = \sqrt{< ROT^2 > - < ROT >^2} \tag{6}$$

where the ROT is differential TEC computed at 1-second cadence. Furthermore, we estimate equivalent S_4 by utilizing the SNR measurements, building upon promising results of recent case studies (Rodrigues & Moraes, 2019; Luo et al., 2020). We convert SNR into linear units of intensity $I = 10^{SNR/10}$, then compute the index on running 60-second window. Finally, we account for elevation angle as introduced in Eq. 5.

$$S_4 = \sqrt{\frac{< I^2 > - < I >^2}{< I >^2}} \cdot F(\Theta)^{0.9} \tag{7}$$

Kintner et al (Kintner et al., 2007) discussed signal Intensity – SNR relationship, where SNR is averaged over a period of 1 second. The exact formulation used by receiver types used in this study is unknown. On one hand, the introduced technique for S_4 estimation has been proven to correlate well with conventional S_4 computed directly from the signal intensity (Thompson et al., 2008; Rodrigues & Moraes, 2019; Luo et al., 2020). On the other hand, the primary drawback of using SNR is a fade smearing due to the temporal averaging, as demonstrated by Jiao et al. (Jiao et al., 2016).

2.2 Event definition

We have discussed data impairments and mitigation of geodetic receivers used in the UNAVCO network. Here we discuss "scintillation event" selection procedure, that takes into account inherent noise level variability due to diverse receiver hardware selection. In the event selection criteria, we build upon Jiao et al. (Jiao & Morton, 2015) statistical survey, with additional receiver specific factor. Figure 3 presents a distribution of receiver hardware set-ups and related histogram of noise levels of the introduced indices. We chose to use a daily median value of phase $\widehat{\sigma_{TEC}}$, and amplitude $\widehat{SNR_4}$ scintillation index, as a measure of receiver noise floor. We compute statistical distribution of these levels on a full month of January 2018, excluding days with planetary K (Kp) index $Kp \geq 4$ (14th and 24th of January). All receivers were located in the northern hemisphere, where the total background TEC is the lowest on yearly basis. Figure 3a depicts average hardware distribution in the time period of this analysis. Figure 3b shows a distribution of receiver noise levels among all available receivers. Figure 3c breaks down the receiver noise levels for each receiver set-up. Overall, both $\widehat{\sigma_{TEC}}$ and $\widehat{SNR_4}$ have

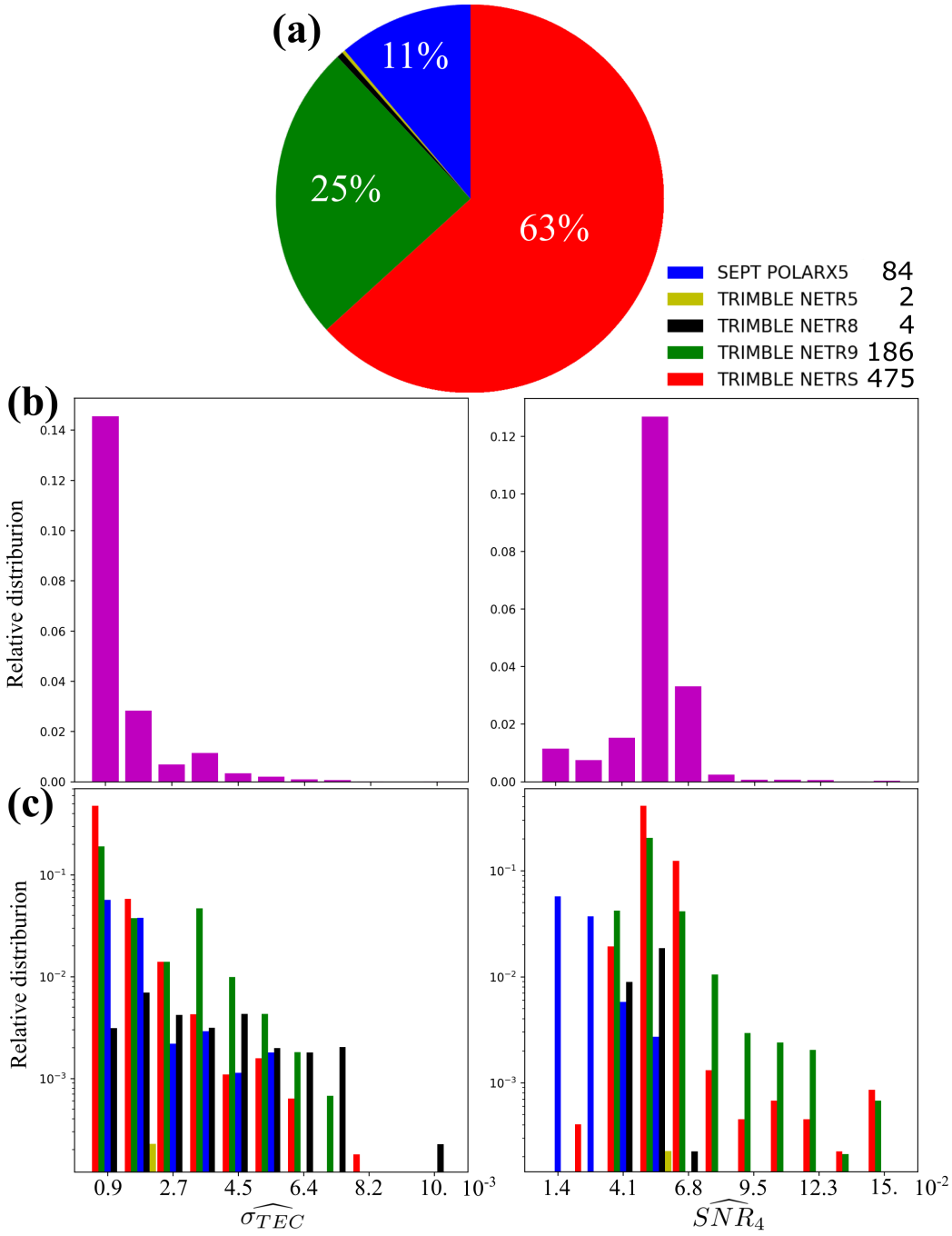

Figure 3. (a) Average receiver hardware availability-distribution in January 2018. (b) Histogram of daily median σ_{TEC} distribution (left), and daily median SNR_4 distribution (right) among all receivers in January 2018. (c) The same as panel (b), but for each hardware set-up.

a large spread with a factor of ∼5 in σ_{TEC}, and a factor of ∼10 in SNR_4. While the degree of spread in σ_{TEC} is similar among different receiver set-ups, with the worst performer being Trimble NETR8, Septentrio PolaRX5 is notably a receiver with the smallest noise level and variance in SNR.

To cope with receiver-dependent noise levels, we define a threshold parameter T^r_χ, for $\chi \in [\sigma_{TEC}, SNR_4]$, for each receiver r computed on a daily basis. The threshold values are defined as:

$$T^r_\chi = 2.5 \cdot \widehat{\chi}^r \tag{8}$$

where a value of 2.5 is a fix standoff distance from the receiver noise level $\widehat{\chi}^r$. Although this number is empirically chosen, as demonstrated below, this threshold effectively separate real scintillation signal and noise. Scintillation events are then defined separately for σ_{TEC} and SNR_4 as follows: Running median (60 s length) value of a scintillation index has to continuously exceed the computed threshold Eq. 8 for a minimum duration of 2 minutes. Additionally, multiple events with temporal separation shorter than 5 minutes are merged together. The introduction of the variable threshold value T^r_χ depending on the noise level is a modification from a fixed cutoff method used by Jiao et al. (Jiao & Morton, 2015), because a fixed threshold creates a bias between different types of receivers.

The event selection is pictorially demonstrated in Fig. 4. In Fig. 4a, a system glitch and an amplitude scintillation event occurred within 30 minutes. The top panel shows a sudden increase in SNR by 3 dB at 00:17 universal time (UT), followed by an event of increased variance at 00:45-01:00 UT. The second panel shows the computed SNR_4 index in blue, and its 1 minute running median in red. The black dashed line is the receiver noise level $\widehat{SNR_4}^{wmok}$, and the magenta dashed line is the threshold level $T^{wmok}_{SNR_4}$. The bottom panel, Fig. 4, demonstrates the event selection result by the thick line. The increased SNR_4 due to the system glitch was rejected by the minimum length criterion. In contrary, the event selection procedure flagged elevated SNR_4 between 00:45 and 1:00 UT as a scintillation event.

The second example in Fig. 4b depicts a case of a long-lasting phase scintillation event co-located with a TEC gradient at 0:40-1:30 UT. There was a secondary enhancement in the σ_{TEC} around 2:00 UT. Because of the minimum separation criterion, we consider the two individual events as a single continuous event, since the gap between the two events was shorter than 5 minutes.

3 Case study

We analyze and validate the introduced indices, and scintillation event selection on an event study. We have processed six days worth of data surrounding the 7-8 September 2017 geomagnetic storm. The solar wind and geomagnetic indices for this time period (5th to 11th September 2017) are presented in Figure 5. The solar wind data show that two consecutive shocks hit the magnetopause on the 7th September, with a time separation of about 24 hours. While the first shock arrived with predominantly northward interplanetary magnetic field (IMF), the latter one was accompanied by a strong (∼-30 nT) southward IMF. The latter shock facilitated enhancement of the ring current (SYM/H index), and increased high-latitude geomagnetic activity measured by auroral electrojet (AE) index. There were two episodic AE intensifications on 8th September; both were related to storm development (negative excursion of the SYM/H).

The storm was particularly intriguing, as it severely perturbed the ionosphere at the longitude sector of northern America, and thus it was well sampled by the UNAVCO GPS network. The ionosphere exhibited several distinct perturbations at this local time sector, in the form of equatorial plasma bubbles (EPBs), severe auroral activity, and multiple TEC gradients at mid-latitudes (over CONUS). Impulsive perturbations have been

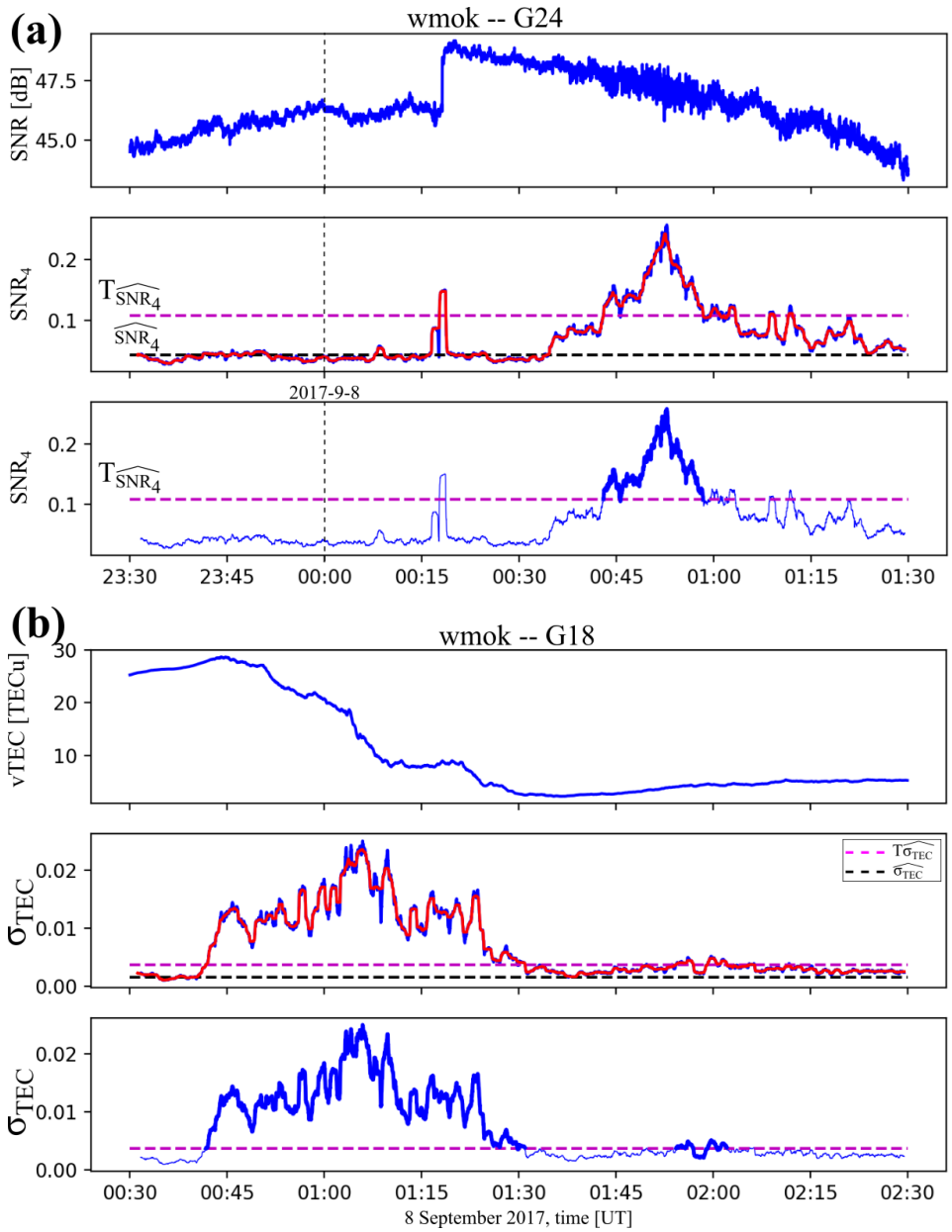

Figure 4. Scintillation event diagnostic. Dashed lines present threshold values (magenta), and receiver noise level (black). Scintillation events are bolstered in the bottom panel of each example. (a) Demonstration of system glitch rejection and amplitude scintillation event. (b) Demonstration of phase scintillation event, and merger of two events separated for less than 5 minutes.

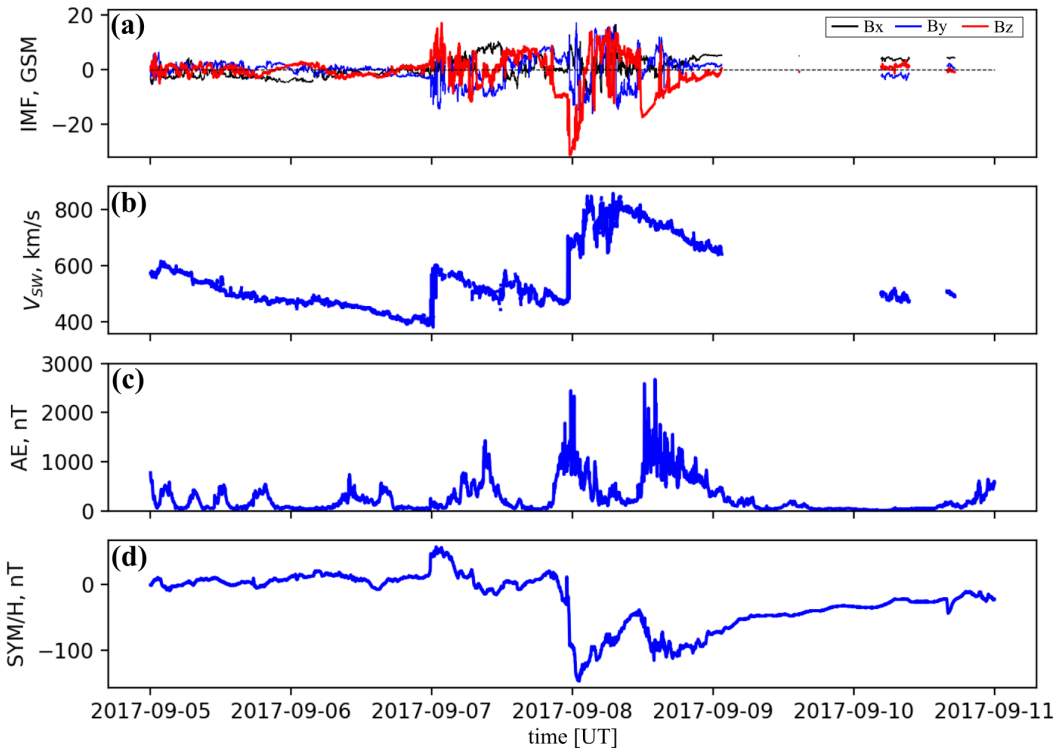

Figure 5. OMNIweb solar wind and geomagnetic indices from for the time period between 5-11 September 2017. (a) Interplanetary magnetic field components in GSM coordinates. (b) Solar wind speed. (c) Auroral electrojet (AE) index. (d) Ring current strength proxy via SYM/H index.

Table 1. A subset of receivers (Rx) – satellites (SV) links under examination

Rx name	GLON	GLAT	receiver model	SV (blue, orange, magenta)
CN12	-76.7	18	Trimble NETR9	G18, G21, G26
HDIL	-89.3	40.6	Septentrio PolaRx5	G18, G21, G32
OXUM	-96.5	15.7	Trimble NETR9	G16, G22, G26
P209	-122.1	37.1	Trimble NETRS	G10, G14, G32
P413	-120.1	48.4	Trimble NETRS	G10, G14, G32
WMOK	-98.8	34.7	Septentrio PolaRx5	G18, G31, G32

reported (Aa et al., 2019; Zakharenkova & Cherniak, 2020; Mrak et al., 2020), but small-scale density irregularity distribution remains unknown, due to the lack of scintillation receivers. Severe space weather impact on GNSS have been reported over contiguous U.S., (Yang et al., 2020), however, associated scintillation or small-scale irregularities haven't been yet reported. We take advantage of the UNAVCO GPS receivers and demonstrate the scintillation processing for this event.

3.1 Evaluation of scintillation indices and event selection

We analyze scintillation indices computed from a subset of six-receivers during the time frame of 7-8 September storm main phase. The chosen receivers are listed in Ta-

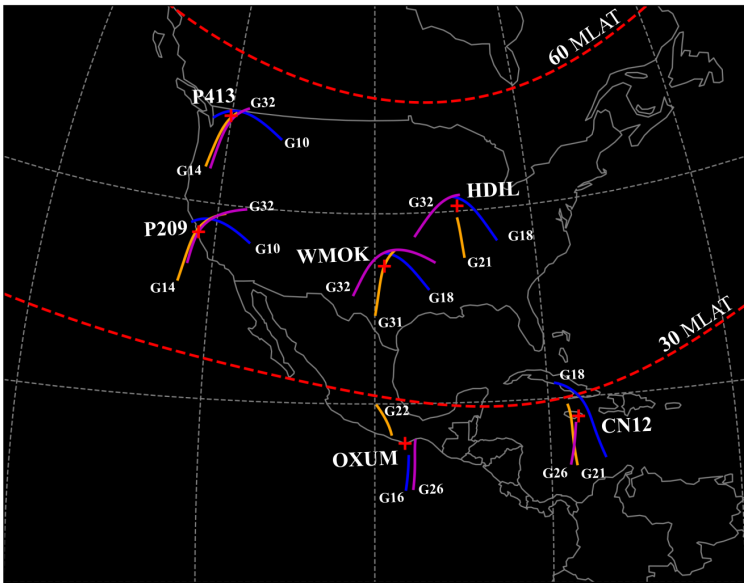

Figure 6. Locations of receivers from Table 1, with trajectories of ionospheric piercing points from the chosen satellites.

ble 1, and we focus only on three most affected lines-of-sight for each of the receivers. The corresponding trajectories of ionospheric pierce points (IPPs) at 350 km altitude are depicted in Fig. 6 for the time period shown in the Fig. 7. Derived TEC and scintillation indices for these receivers are presented in Fig. 7. Receivers are chosen in a way to cover a large span in longitude and latitude, and to present time-series plots of the three most frequency hardware set-ups.

Each panel in Fig. 7 consists of computed TEC (Eq. 1), ROTI and SNR-derived S_4, σ_{TEC} and SNR_4. The TEC plots show dramatic TEC perturbations, some exceeding 10 TECu at time scales of a few minutes. In general, ROTI values correlate well with these gradients, revealing existence of irregularities with temporal scales in the order of 1 second. A comparison between ROTI and σ_{TEC} indicates a linear correlation, showing no morphological differences regardless of the receiver type, and intensity of irregularities. While most of the receivers observed elevated TEC perturbations by virtue of both indices, the event threshold $T_{\sigma_{TEC}} \approx 0.01$ (translates to $\widehat{\sigma_{TEC}} \approx 4 \cdot 10^{-3}$) for all receivers, regardless the receiver type.

The bottom two panels of each receiver in Fig. 7 serve as comparison between amplitude scintillation indices. Like in the TEC case, the indices are visually well correlated, but show strikingly different variance (noise level) among different receivers. A large span in the thresholds T_{SNR_4} is expected based on the preliminary quiet day analysis (Fig. 3). In the given example, Septentrio PolaRx5 receivers (wmok and hdil) have the threshold level a factor of $\sim$2 smaller than Trimble receivers. We find the introduced SNR_4 index has a bigger dynamic range, due to the fact it is not normalized.

Another striking observation is enhanced amplitude scintillation, as four of the receivers were located within CONUS; Washington state (p413), Oklahoma (wmok), Illinois (hdil), and California (p209). Less strikingly, receivers at lower latitudes; Jamaica (cn12) and Mexico (oxum), were as well subject to enhanced scintillation. Specifically, receiver oxum recorded extreme amplitude scintillation with $S_4 \geq$0.5, accompanied by numerous loss-of-locks, which prevented the calculation of σ_{TEC} index. Phase scintillation was co-located with amplitude scintillation at all instances. Receiver p413 mea-

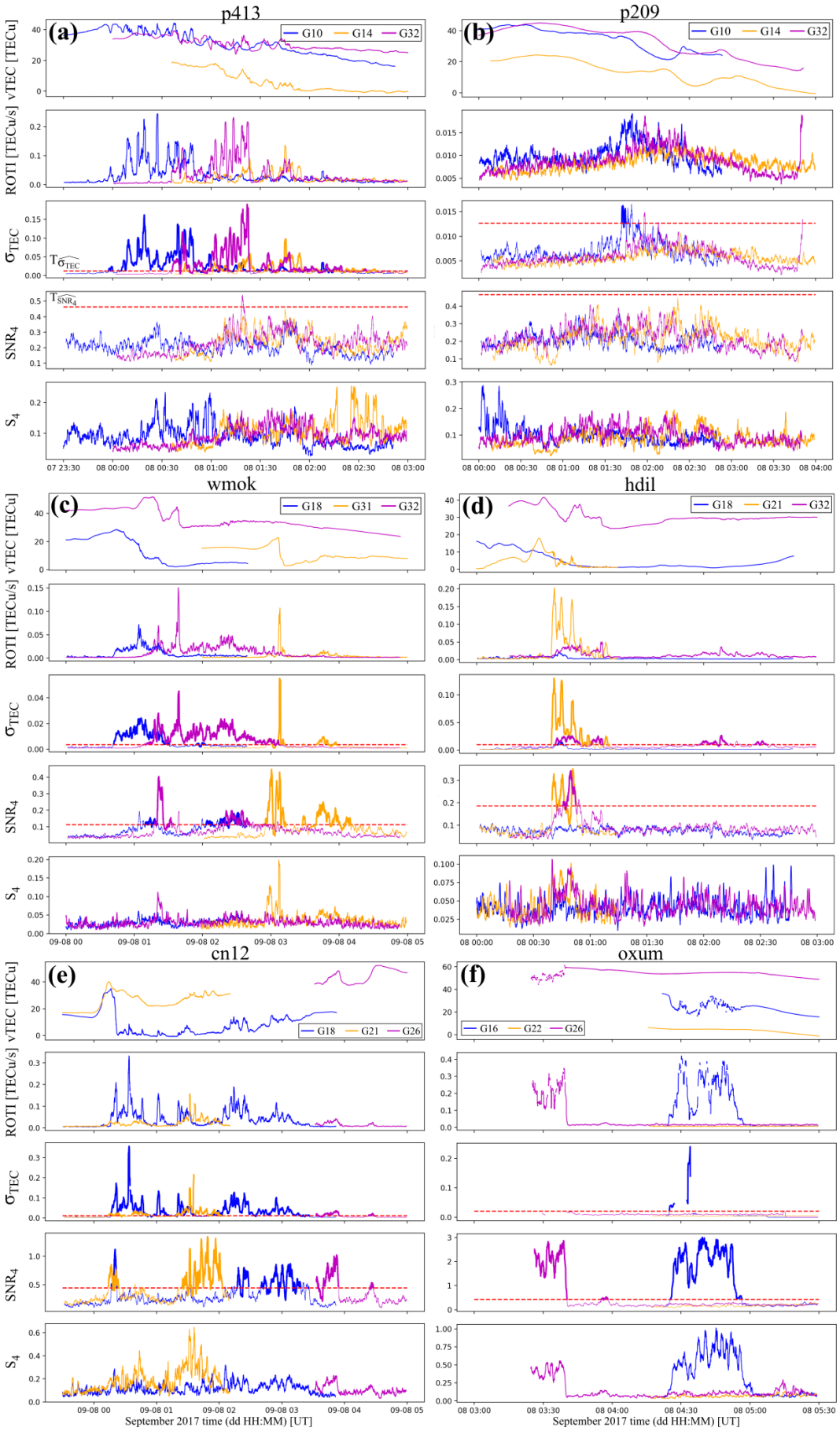

Figure 7. Example measurements from three receivers, introduced in Figure 6. Each panel consist of estimated vTEC, conventional scintillation indices and the introduced alternative indices. Each receiver represents different hardware set-up, presented in Table 1. Red dashed lines are associated the thresholds T_χ^r.

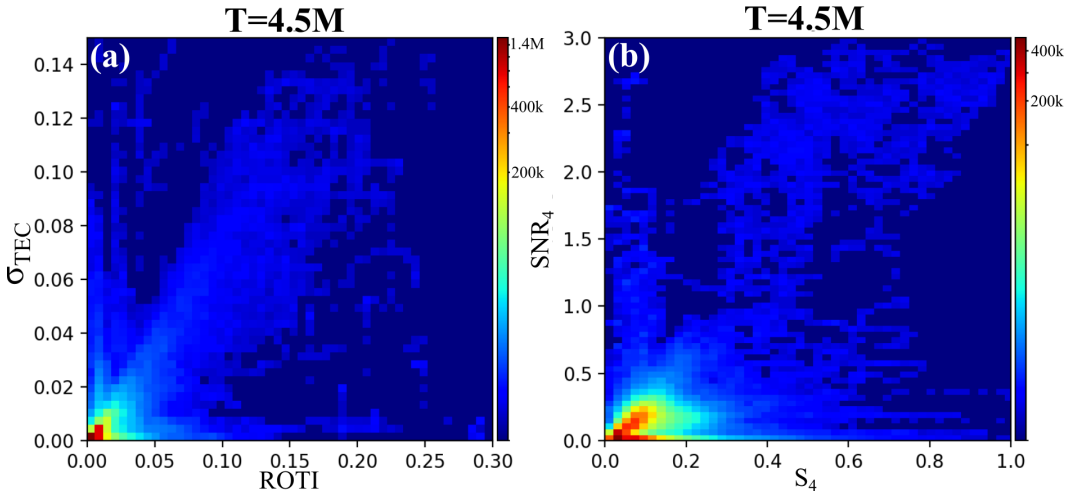

Figure 8. 2D histogram showing direct comparison between conventional and introduced scintillation indices, using data of 6 selected receivers from Table 1. Title contains information about total number of data points T used in the analysis. (a) Comparison between ROTI and σ_{TEC}. (b) Comparison between S_4 and SNR_4.

sured only increased phase scintillation, indicting it got affected by different kinds of ionospheric structures. Lastly, enhanced amplitude scintillation is well correlated with phase scintillation σ_{TEC} and ROTI, generally co-located with the steep TEC gradients.

The correlation between ROTI and σ_{TEC} observed with all receivers is not surprising. As we introduced in the previous section via Eq.1, they should be linearly correlated. The advantages of σ_{TEC} over ROTI are a deterministic amplitude and phase response by the prescribed filtering operation, and a straightforward connection with the TEC power spectral density (PSD_{TEC})

$$\sigma^2_{TEC} = 2 \int_{0.1}^{\infty} PSD_{TEC}(f)\ df, \tag{9}$$

following the morphology derived for phase scintillation (Secan et al., 1995; Béniguel et al., 2009), where the low limit in the integration is a chosen frequency cut-off at 0.1 Hz. Correlation between SNR_4 and σ_{TEC} does exists from cases of measured amplitude scintillation. The latter observation is also expected as several studies demonstrated correlation and casual relationship between ROTI and S_4 (Carrano et al., 2019; Yang & Liu, 2016; Liu & Radicella, 2019). Correlation deviation in this formalism is thought to be due to viewing geometry and irregularity drift velocity (Carrano et al., 2019; Liu & Radicella, 2019).

The importance of the hardware-dependent scintillation event classification is bolstered by means of large scale statistical relationships; σ_{TEC} – ROTI, and SNR_4 – S_4. A mutual comparison between the indices is presented as 2D histograms in Fig. 8. The histograms encompass data from the receivers in Table 1 on a time period of 48 hours (7th and 8th September 2017), with totally ∼4.5 million data points. The histograms show two major populations; a correlated group clustered along a linear correlation line, and the second, uncorrelated group along both axes. The latter group exists due to receiver impairments such as cycle slips, and processing artifacts.

We then apply the scintillation event decision criteria, and re-do the correlation analysis in Fig. 9. Panels (a) show the results from the same data set as in Fig. 8. The criteria effectively rejected the uncorrelated groups, and the results show linear relation-

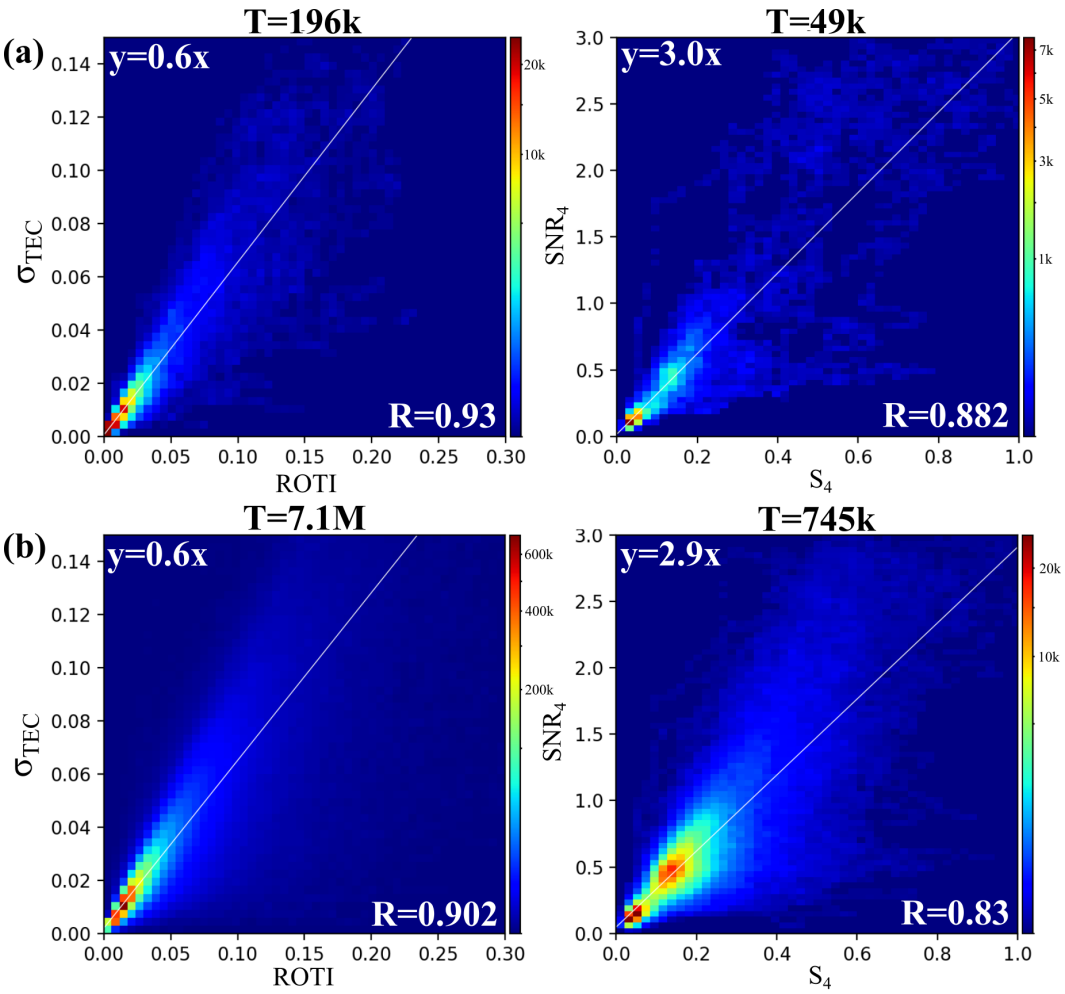

Figure 9. The same format as in Figure 8 but only using data points above the thresholds in equation 8. (a) Using the six selected receivers from Table 1. (b) All selected 169 receivers depicted in Figure 1. The total number of data points T are at the top of each panel. White fiducial line fit to the data with equation in the top left corner. Correlation coefficient R between selected indices is given in the bottom right corner.

ship between both σ_{TEC}–ROTI, and SNR_4 and S_4. Linear correlation with high correlation coefficient indicate that the introduced scintillation indices are adequate substitutes for ROTI and S_4. The bottom panel (b) presents analysis taken from all receivers in Fig. 11 processed in this case study. The linear correlation line is plotted on each panel, including the line parameters, and the correlation coefficient R. We find the correlation coefficient between σ_{TEC} and ROTI R=0.9, and SNR_4 – S_4 R=0.83.

3.2 Comparison against CASES scintillation receiver

We compare measurements from the *wmok* receiver located in Oklahoma with a CASES scintillation receiver (Crowley et al., 2011) deployed at UT Dallas, TX. The receivers are spaced ∼240 km apart. As the UT Dallas receiver was operating only until 2:30 UT on the 8th September, we utilize data recorded in this time period. The CASES receivers sample carrier phase and signal intensity of the L1CA channel at 100 Hz resolution, and output scintillation indices σ_ϕ and S_4 at 100 seconds rate. This rate devi-

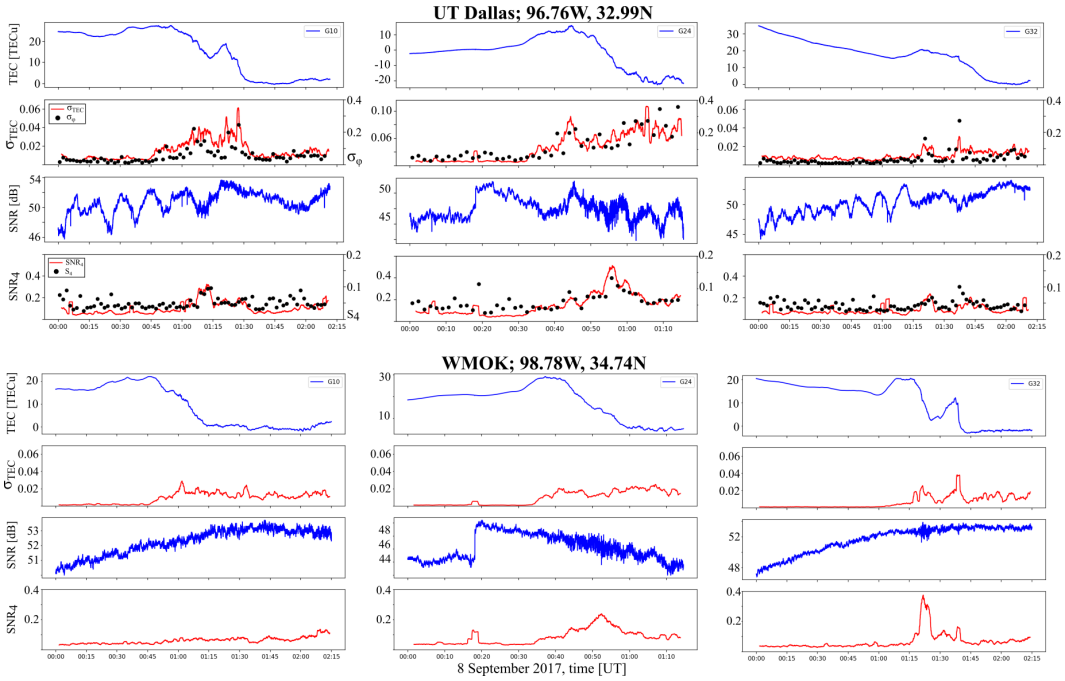

Figure 10. Comparison between observations taken by CASES (top) receiver from Dallas, TX, and wmok receiver from Oklahoma (bottom). Each row consists of three frames of data from G10, G24 and G32 satellites. Top row (CASES) has additional scintillation indices (σ_ϕ, S_4) in the second and bottom panels (respectively). Red lines represent the introduced (σ_{TEC}, SNR_4) scintillation indices.

ates from the conventional approach (60 seconds rate), which is also adopted in this work. Nevertheless, we adopt this method for the *wmok*, to compare the data against each other. CASES receivers provide estimates of the TEC and SNR at 1 second data rate.

We analyze observations from three satellite links, where we derive the introduced scintillation indices (σ_{TEC}, SNR_4) at 100 seconds rate, and compare them with the conventional σ_ϕ and S_4. The comparison is presented in Fig. 10, where the top row consist of frames with observations taken by CASES receivers, and the bottom row of the *wmok*. Estimated TEC is plotted in the top panel, whereas the derived σ_{TEC} is in the second panel. It is plotted side-by-side with the phase scintillation index σ_ϕ. All three lines-of-sight show that σ_{TEC} follows the dynamics of σ_ϕ, for each of the scintillating events. Bottom two panels show the SNR in the third panel, whereas the SNR_4 and S_4 indices are in the last panel. The latter amplitude scintillation indices have large variance owing to receiver's performance, as indicated by large variations in the SNR panels. The SNR_4 index, derived from the SNR, however generally follow the trend of the S_4 which was derived from 100 Hz signal intensity measurements.

The general trend in the scintillation indices (red lines) is morphologically similar between both receivers. While the middle frames, monitoring satellite G24, show almost identical trends in both σ_{TEC} and SNR_4, the other links have a distinct difference. The difference originates in different electron density structure as measured by the TEC. Altgough the receivers were apart ~240 km, one measures step-like gradient in TEC, whereas the other a single TEC descend. A promising observation, however, is that in either case of the double-slope gradient, both receivers measured increased amplitude scintillation in the plateau region between the density gradients. This was measured by the CASES

receiver in the G10 link at ∼1:15 UT, and by the *wmok* at about the same time. It should be noted that despite that increased variance in raw SNR data, namely amplitude scintillation, is clearly observed, the value of the scintillation index S_4 is below 0.2 usually used as a scintillation detection threshold (Jiao & Morton, 2015; Béniguel et al., 2009).

In aggregate, the CASES scintillation receiver provides independent validation for the introduced phase scintillation index substitute, σ_{TEC} that follows the trend of σ_ϕ. Additionally, CASES derived amplitude scintillation index S_4 measured instances of elevated amplitude scintillation, which were also indicated by the SNR-derived SNR_4. In comparison with the closest UNAVCO receiver, it is found that both receivers measured the same scintillating structures, both with phase σ_{TEC} and amplitude SNR_4 scintillation indices.

3.3 Scintillation maps and event analysis

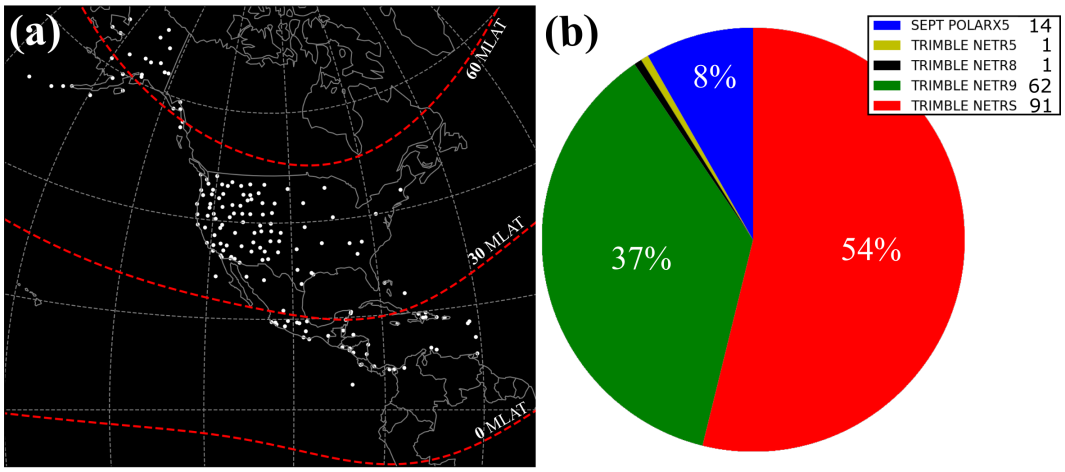

Figure 11. Same format as Fig. 1, with spatial distribution of receivers chosen (total of 169) to produce irregularity maps in this case study.

A spatiotemporal evolution of the scintillation indices during the storm is obtained by virtue of scintillation maps from chosen receivers presented in Fig. 11. A total number of 169 receivers was selected based on the criteria to reduce receiver density to 1 receiver per 2°GLON × 2°GLAT bin. Total number and specific receiver hardware contribution to the subset of the receiver network is presented in the Fig. 11b. We present the irregularity maps in Fig. 12, covering the 7-8 September storm at a time resolution of 1 hour. Irregularity maps consist of σ_{TEC} and SNR_4 indices, which are compared to the ROTI maps at each epoch. Each frame consists of data points collected in the first 5 minutes after the image time-stamp.

The maps in Fig. 12 show how well the regions of elevated ROTI correlate with scintillation occurrence. At the beginning of the storm main phase in Fig 12a, the area with high ROTI overlapping predominant phase scintillation σ_{TEC} lies within a storm enhanced density plume extending from central US up to northern Alaska. In the next frame, morphology of the scintillation at the poleward portion of the CONUS network remains unchanged, while a meridional density depletion over eastern US, the secondary density trough (see Mrak et al. (Mrak et al., 2020)) is associated with enhanced ROTI and both amplitude and phase scintillation.

An hour later in Fig. 12c the maps show a change in scintillation morphology in vicinity of mid-latitude trough located near the US-Canada border. There are two dis-

tinct meridionally separated scintillation regions there; one poleward in the area of elevated density (the auroral oval), and the other one equatorward of the trough. The scintillation elongated along the secondary density trough persisted through the last hour. Additionally, there are numerous instances of observed amplitude scintillation within the secondary trough, as previously presented in time-series plot of receiver p413 in Fig. 7d. The scintillation lingered over the CONUS area for at least another hour (panels d), before they began to dissipate away.

Another region of intense amplitude scintillation emerged at about 1:30 universal time (UT) (Fig. 12d), located within the high density area near 20°MLAT, just west of 0° magnetic longitude meridian. Amplitude scintillation, accompanied with phase scintillation (in conjunction with elevated ROTI) persisted until the end of the event analysis at 4:30 UT. The scintillation geolocation deep within the high density (the equatorial ionization anomaly), in conjunction with timing (pre-midnight local time) strongly suggest the scintillation was a consequence of equatorial plasma bubbles (Béniguel et al., 2009). At the same time, high-latitude activity was strictly confined within the auroral oval, over the Alaskan sector.

Lastly, we analyze total scintillation occurrence during the time period of six days surrounding the storm under investigation. We present time-series of scintillation occurrence in Fig. 13. We present data from all receivers chosen in this study, introduced in Fig. 11. As a reference, we plot the ROTI in the top panel; the time-series consist of instantaneous median of all ROTI samples among all the lines-of-sight. The scintillation indices from all receivers are presented in a normalized fashion, where a temporal median value is normalized by a total number of scintillation events (N) recorded at that time. Normalization here is necessary due to the event selection, resulting in variable number of available samples at a given time. Resulting normalized phase scintillation $\sigma_{TEC} \cdot N$, and amplitude scintillation $SNR_4 \cdot N$ are plotted in the bottom two panels.

The phase scintillation occurrence in Fig. 13b has three distinct peaks, which correlate well with auroral electrojet (AE index) intensifications in the background. The correlation is expected as the AE is a proxy measure of auroral activity which is well established as the predominant source of phase scintillation at high-latitudes. The second increase in σ_{TEC}, however, is disproportional to the AE enhancement, but is also correlated with extreme increase in amplitude scintillation SNR_4, shown in the bottom panel Fig. 13c. The latter increase occurred at the dip of the geomagnetic storm, indicated by the negative deflection in SYM/H index. Finally, both indices correlate well with ROTI maps, however, the other two instances of elevated phase scintillation index σ_{TEC} do not show contemporary increase in the median ROTI. This is due to the fact that only a localized area of the receiver network coverage experienced the scintillation, hence the elevated ROTI, and the use of a median operator did not pick up the increases in ROTI which did not undergo the scintillation event classification decision process.

4 Summary and conclusions

We have introduced an alternative method to obtain ionospheric scintillation indices from geodetic GPS receivers with 1 Hz data rate. We have discussed limitations imposed by opportunistic data source, which has limited temporal sampling range. We have introduced and demonstrated the efficiency of a hardware-dependent scintillation event classification by virtue of direct comparison with ROTI and SNR-derived S_4. We showed that the introduced amplitude scintillation SNR_4 index is more sensitive to weak events (cf. Fig. 7) than the S_4, due to the fact the SNR_4 is not normalized. The introduced phase scintillation index σ_{TEC} show linear correlation with ROTI, with a correlation coefficient 0.902. Another property of the introduced scintillation indices is equal signal processing treatment, where the filtering function has a deterministic impulse response, in contrary to the ROT and ROTI.

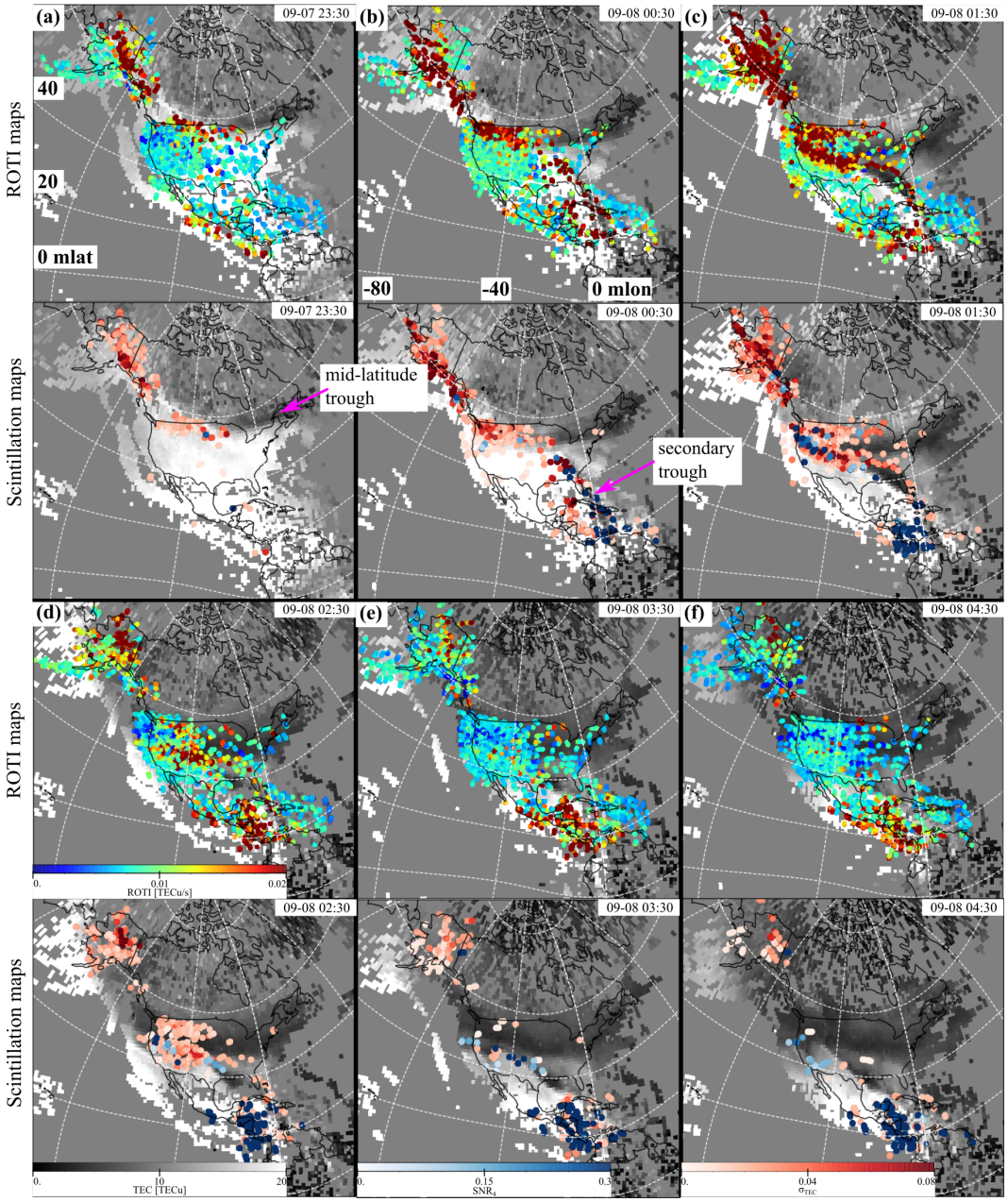

Figure 12. ROTI and scintillation maps for a time period of the storm main phase. Each epoch panel consists of two vertically stacked maps; ROTI on top, and the Scintillation indices in the bottom map. The ROTI and scintillation indices are overlaid on top of the TEC maps. Grid lines are in geomagnetic coordinates.

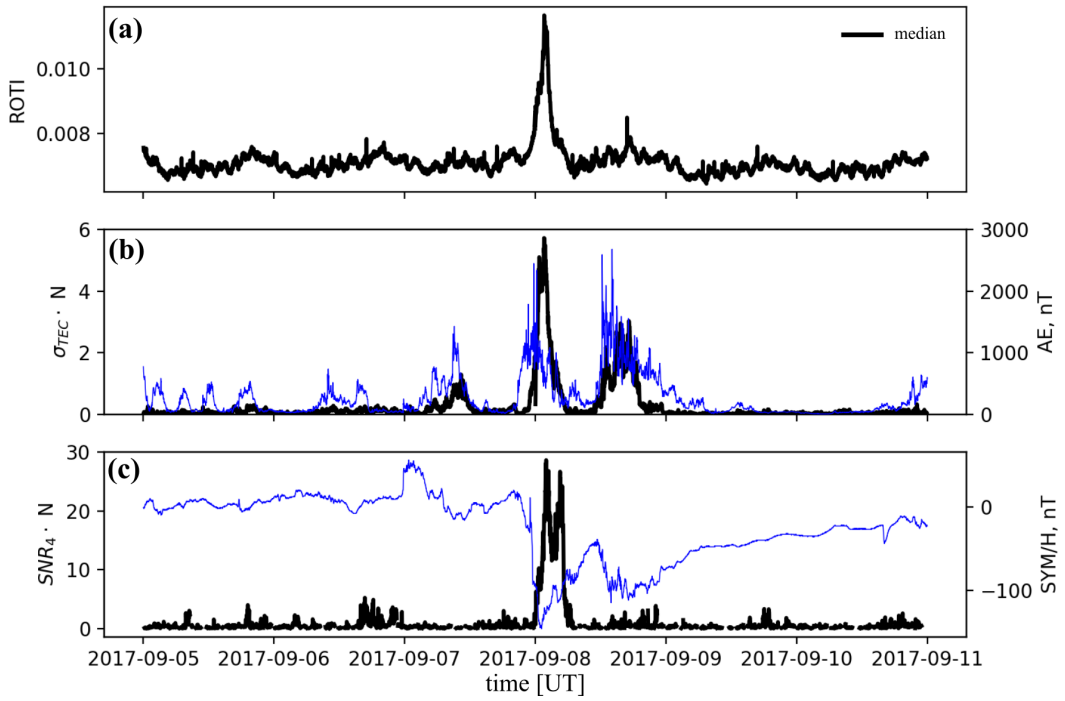

Figure 13. Scintillation indices time-series plots from all available receivers, for the time period of surrounding the 7-8 geomagnetic storm. (a) ROTI time series represented by instantaneous median value (black). (b) Median σ_{TEC} value normalized by total number of events N ($\sigma_{TEC} \cdot N$). (c) Median SNR_4 value normalized by total number of instantaneous scintillation events N ($SNR_4 \cdot N$).

The introduced processing was applied to the UNAVCO GPS dataset, we leveraged its large spatial coverage to produce scintillation maps. The most profound virtue of large spatial coverage in the ability to examine scintillation evolution at a continental scale covering longitude sector of the CONUS. We demonstrated the potential importance of the data product on a case study of the 7-8 September 2017 storm. The results reveal episodic scintillation occurrence and spatiotemporal evolution in an area covering over 50°MLAT, considered to be primarily within the mid-latitude ionosphere. Long term observation of scintillation occurrence shows a good correlation between increased auroral activity and the phase scintillation index σ_{TEC}. A disproportional increase in both phase and amplitude scintillation was observed during the storm main phase. Spatiotemporal evolution of the scintillation geolocation, was analyzed by virtue of scintillation maps. Namely, high latitude scintillation was predominantly confined to the area within the auroral oval and in the vicinity of the trough equatorward boundary, characterized by an elevated phase scintillation index. Because this region lacks amplitude scintillation, the elevated phase scintillation index is likely due to phase variations associated with fast moving density structures. Low latitude scintillation was predominantly confined within the equatorial ionization anomaly at pre-midnight local time sector, consisting of both elevated amplitude and phase scintillation, a morphology of Fresnel scatter. Lastly, additional large scale density trough was located predominantly at mid-latitudes, and was associated with elevated amplitude and phase scintillation. The latter finding is a novel observation, made available by the utilization of geodetic receivers.

The presented case of storm time spatial evolution of GPS scintillation at mid-latitudes shed a new light on past observations of scintillation from upstate New York (Ledvina

et al., 2002). Additionally, the promising results of scintillation event classification and demonstrated utility of scintillation maps allow a comprehensive retrospective analysis of thus far ignored scintillation occurrence at mid-latitudes. The data availability goes back to 2011, as a statistical survey is currently underway. While scintillation occurrence at low- and high-latitudes agree well with established scintillation climatology (Kintner et al., 2007; Aarons, 1982; Basu et al., 1988; Secan et al., 1995, 1997; Béniguel et al., 2009), the preliminary results from receivers at mid-latitudes partially agree with historical morphology of mid-latitude scintillation (Kintner et al., 2007; Aarons, 1982). That is, an increase of phase scintillation is predominantly due to TEC gradients in the vicinity of the trough equatorward boundary, and increased plasma convection within the trough. The results of the presented case study indicate there are other mid-latitude mechanisms producing both amplitude and phase scintillation. The climatology and controlling parameters of these events are mysterious, as it appears they occur during large storms (Ledvina et al., 2002; Aa et al., 2019; Zakharenkova & Cherniak, 2020). Leveraging 1 Hz geodetic receivers, such as the one operated by UNAVCO, could be utilized to gain insight into the mid-latitude scintillation phenomenon through a comprehensive retrospective analysis.

Acknowledgments

The study was supported by NSF-AGS 1821135, NSF-AGS-1907698, NASA-0NSSC18K0657, and AFOSR FA9559-16-1-0364 awards to Boston University. F. S. Rodrigues would like to thank support from NSF-AGS-1554926. This data product was fostered by the NASA Living With a Star Institute 2019, Mid-latitude Irregularities and Scintillation. GPS data is freely available at

ftp://data-out.unavco.org/pub/highrate/1-Hz/rinex/. GPS TEC maps were retrieved via publicly http://cedar.openmadrigal.org/. Solar wind and geomagnetic indices are available via OMNI database https://cdaweb.sci.gsfc.nasa.gov/pub/data/omni/.

References

Aa, E., Zou, S., Ridley, A., Zhang, S., Coster, A. J., Erickson, P. J., ... Ren, J. (2019). Merging of Storm Time Midlatitude Traveling Ionospheric Disturbances and Equatorial Plasma Bubbles. *Space Weather*, *17*(2), 285–298. doi: 10.1029/2018SW002101

Aarons, J. (1982). Global morphology of ionospheric scintillations. *Proceedings of the IEEE*, *70*(4), 360–378. Retrieved from `http://ieeexplore.ieee.org/document/1456582/` doi: 10.1109/PROC.1982.12314

Alfonsi, L., Spogli, L., De Franceschi, G., Romano, V., Aquino, M., Dodson, A., & Mitchell, C. N. (2011). Bipolar climatology of GPS ionospheric scintillation at solar minimum. *Radio Science*, *46*(3), 1–21. doi: 10.1029/2010RS004571

Basu, S., MacKenzie, E., & Basu, S. (1988, may). Ionospheric constraints on VHF/UHF communications links during solar maximum and minimum periods. *Radio Science*, *23*(3), 363–378. Retrieved from `http://doi.wiley.com/10.1029/RS023i003p00363` doi: 10.1029/RS023i003p00363

Beach, T. L. (2006, nov). Perils of the GPS phase scintillation index (σ ϕ). *Radio Science*, *41*(5), RS5S31. Retrieved from `http://doi.wiley.com/10.1029/2005RS003356http://files/260/rds5269.pdf` doi: 10.1029/2005RS003356

Béniguel, Y. (2002, jun). Global Ionospheric Propagation Model (GIM): A propagation model for scintillations of transmitted signals. *Radio Science*, *37*(3), 4–1–4–13. Retrieved from `http://doi.wiley.com/10.1029/2000RS002393` doi: 10.1029/2000RS002393

Béniguel, Y., Adam, J. P., Jakowski, N., Noack, T., Wilken, V., Valette, J. J., ... Arbesser-Rastburg, B. (2009). Analysis of scintillation recorded during the PRIS measurement campaign. *Radio Science*, *44*(5), 1–11. doi:

10.1029/2008RS004090

Blewitt, G. (1990, mar). An Automatic Editing Algorithm for GPS data. *Geophysical Research Letters*, *17*(3), 199–202. Retrieved from http://doi.wiley.com/10.1029/GL017i003p00199 doi: 10.1029/GL017i003p00199

Carrano, C. S., Groves, K. M., & Rino, C. L. (2019). On the Relationship Between the Rate of Change of Total Electron Content Index (ROTI), Irregularity Strength (C k L), and the Scintillation Index (S 4). *Journal of Geophysical Research: Space Physics*, *124*(3), 2099–2112. doi: 10.1029/2018JA026353

Crowley, G., Bust, G. S., Reynolds, A., Azeem, I., Wilder, R., O'Hanlon, B. W., ... Bhatti, J. A. (2011). CASES: A novel low-cost ground-based dual-frequency GPS software receiver and space weather monitor. *24th International Technical Meeting of the Satellite Division of the Institute of Navigation 2011, ION GNSS 2011*, *2*, 1437–1446.

Fremouw, E. J., Leadabrand, R. L., Livingston, R. C., Cousins, M. D., Rino, C. L., Fair, B. C., & Long, R. A. (1978, jan). Early results from the DNA Wideband satellite experiment-Complex-signal scintillation. *Radio Science*, *13*(1), 167–187. Retrieved from http://doi.wiley.com/10.1029/RS013i001p00167 doi: 10.1029/RS013i001p00167

ITUR-P.531-14. (2019). Recommendation, ionospheric propagation data and prediction methods required for the design of satellite networks and systems, geneva.

Jiao, Y., & Morton, Y. T. (2015, sep). Comparison of the effect of high-latitude and equatorial ionospheric scintillation on GPS signals during the maximum of solar cycle 24. *Radio Science*, *50*(9), 886–903. Retrieved from https://onlinelibrary.wiley.com/doi/abs/10.1002/2015RS005719 doi: 10.1002/2015RS005719

Jiao, Y., Xu, D., Morton, Y., & Rino, C. (2016, sep). Equatorial Scintillation Amplitude Fading Characteristics Across the GPS Frequency Bands. *Navigation*, *63*(3), 267–281. Retrieved from http://doi.wiley.com/10.1002/navi.146 doi: 10.1002/navi.146

Juan, J. M., Aragon-Angel, A., Sanz, J., González-Casado, G., & Rovira-Garcia, A. (2017, nov). A method for scintillation characterization using geodetic receivers operating at 1 Hz. *Journal of Geodesy*, *91*(11), 1383–1397. Retrieved from http://link.springer.com/10.1007/s00190-017-1031-0 doi: 10.1007/s00190-017-1031-0

Kintner, P. M., Ledvina, B. M., & de Paula, E. R. (2007, sep). GPS and ionospheric scintillations. *Space Weather*, *5*(9), n/a–n/a. Retrieved from http://doi.wiley.com/10.1029/2006SW000260http://files/178/rds1552.pdfhttp://files/248/rds1992.pdfhttp://files/247/swe177.pdf doi: 10.1029/2006SW000260

Ledvina, B. M., Makela, J. J., & Kintner, P. M. (2002, jul). First observations of intense GPS L1 amplitude scintillations at midlatitude. *Geophysical Research Letters*, *29*(14), 4–1–4–4. Retrieved from http://doi.wiley.com/10.1029/2002GL014770http://files/1406/Ledvinaetal.-2002-FirstobservationsofintenseGPSL1amplitudesci.pdf doi: 10.1029/2002GL014770

Liu, Y., & Radicella, S. (2019). On the correlation between ROTI and S4. *Annales Geophysicae Discussions*(November), 1–14. doi: 10.5194/angeo-2019-147

Luo, X., Gu, S., Lou, Y., Cai, L., & Liu, Z. (2020). Amplitude scintillation index derived from C / N 0 measurements released by common geodetic GNSS receivers operating at 1 Hz. *Journal of Geodesy*, *123*. Retrieved from https://doi.org/10.1007/s00190-020-01359-7 doi: 10.1007/s00190-020-01359-7

McCaffrey, A. M., & Jayachandran, P. T. (2019, feb). Determination of the Refractive Contribution to GPS Phase "Scintillation". *Journal of Geophysical Research: Space Physics*, *124*(2), 1454–1469. Retrieved from

https://onlinelibrary.wiley.com/doi/abs/10.1029/2018JA025759 doi: 10.1029/2018JA025759

Mrak, S., J., S., Y., N., J.C, F., R., H. M., & W.A., B. (2020). Modulation of storm-time mid-latitude ionosphere by magnetosphere-ionosphere coupling. *JGR: Space Physics, in review*.

Mrak, S., Semeter, J., Hirsch, M., Starr, G., Hampton, D., Varney, R. H., ... Pankratius, V. (2018, jan). Field-Aligned GPS Scintillation: Multisensor Data Fusion. *Journal of Geophysical Research: Space Physics*, *123*(1), 974–992. doi: 10.1002/2017JA024557

Nguyen, V. K., Rovira-Garcia, A., Juan, J. M., Sanz, J., González-Casado, G., La, T. V., & Ta, T. H. (2019, oct). Measuring phase scintillation at different frequencies with conventional GNSS receivers operating at 1 Hz. *Journal of Geodesy*, *93*(10), 1985–2001. Retrieved from https://doi.org/10.1007/s00190-019-01297-zhttp://link.springer.com/10.1007/s00190-019-01297-z doi: 10.1007/s00190-019-01297-z

Pi, X., Mannucci, A. J., Lindqwister, U. J., & Ho, C. M. (1997, sep). Monitoring of global ionospheric irregularities using the Worldwide GPS Network. *Geophysical Research Letters*, *24*(18), 2283–2286. doi: 10.1029/97GL02273

Priyadarshi, S. (2015, mar). A Review of Ionospheric Scintillation Models. *Surveys in Geophysics*, *36*(2), 295–324. Retrieved from http://link.springer.com/10.1007/s10712-015-9319-1 doi: 10.1007/s10712-015-9319-1

Rideout, W., & Coster, A. (2006, jul). Automated GPS processing for global total electron content data. *GPS Solutions*, *10*(3), 219–228. Retrieved from http://link.springer.com/10.1007/s10291-006-0029-5http://files/269/6l6882t7t21337t7.pdf doi: 10.1007/s10291-006-0029-5

Rino, C. L. (1979, nov). A power law phase screen model for ionospheric scintillation: 1. Weak scatter. *Radio Science*, *14*(6), 1135–1145. Retrieved from http://doi.wiley.com/10.1029/RS014i006p01135 doi: 10.1029/RS014i006p01135

Rodrigues, F. S., & Moraes, A. O. (2019). ScintPi: A Low-Cost, Easy-to-Build GPS Ionospheric Scintillation Monitor for DASI Studies of Space Weather, Education, and Citizen Science Initiatives. *Earth and Space Science*, *6*(8), 1547–1560. doi: 10.1029/2019EA000588

Secan, J. A., Bussey, R. M., Fremouw, E. J., & Basu, S. (1995, may). An improved model of equatorial scintillation. *Radio Science*, *30*(3), 607–617. Retrieved from http://doi.wiley.com/10.1029/94RS03172 doi: 10.1029/94RS03172

Secan, J. A., Bussey, R. M., Fremouw, E. J., & Basu, S. (1997, jul). High-latitude upgrade to the Wideband ionospheric scintillation model. *Radio Science*, *32*(4), 1567–1574. Retrieved from http://doi.wiley.com/10.1029/97RS00453 doi: 10.1029/97RS00453

Spogli, L., Alfonsi, L., De Franceschi, G., Romano, V., Aquino, M. H. O., & Dodson, A. (2009, sep). Climatology of GPS ionospheric scintillations over high and mid-latitude European regions. *Annales Geophysicae*, *27*(9), 3429–3437. Retrieved from https://www.ann-geophys.net/27/3429/2009/ doi: 10.5194/angeo-27-3429-2009

Thompson, R. J. R., Cetin, E., & Dempster, A. G. (2008). Detecting Amplitude Scintillation Using C / N 0 Differences.

Wernik, A., Secan, J., & Fremouw, E. (2003, jan). Ionospheric irregularities and scintillation. *Advances in Space Research*, *31*(4), 971–981. Retrieved from https://linkinghub.elsevier.com/retrieve/pii/S0273117702007950 doi: 10.1016/S0273-1177(02)00795-0

Yang, Z., & Liu, Z. (2016). Correlation between ROTI and Ionospheric Scintillation Indices using Hong Kong low-latitude GPS data. *GPS Solutions*, *20*(4), 815–824. doi: 10.1007/s10291-015-0492-y

Yang, Z., Mrak, S., & Morton, Y. (2020). Geomagnetic storm induced mid-latitude

ionospheric plasma irregularities and their implications for gps positioning over north america: A case study. *In proceedings of ION PLANS 2020, Institute of Navigation*.

Yeh, & Liu. (1982). Radio wave scintillations in the ionosphere. *Proceedings of the IEEE*, *70*(4), 324–360. Retrieved from `https://ieeexplore.ieee.org/document/1456581` doi: 10.1109/PROC.1982.12313

Zakharenkova, I., & Cherniak, I. (2020, feb). When Plasma Streams Tie up Equatorial Plasma Irregularities with Auroral Ones. *Space Weather*, *18*(2). Retrieved from `https://onlinelibrary.wiley.com/doi/abs/10.1029/2019SW002375` doi: 10.1029/2019SW002375

Figure1.

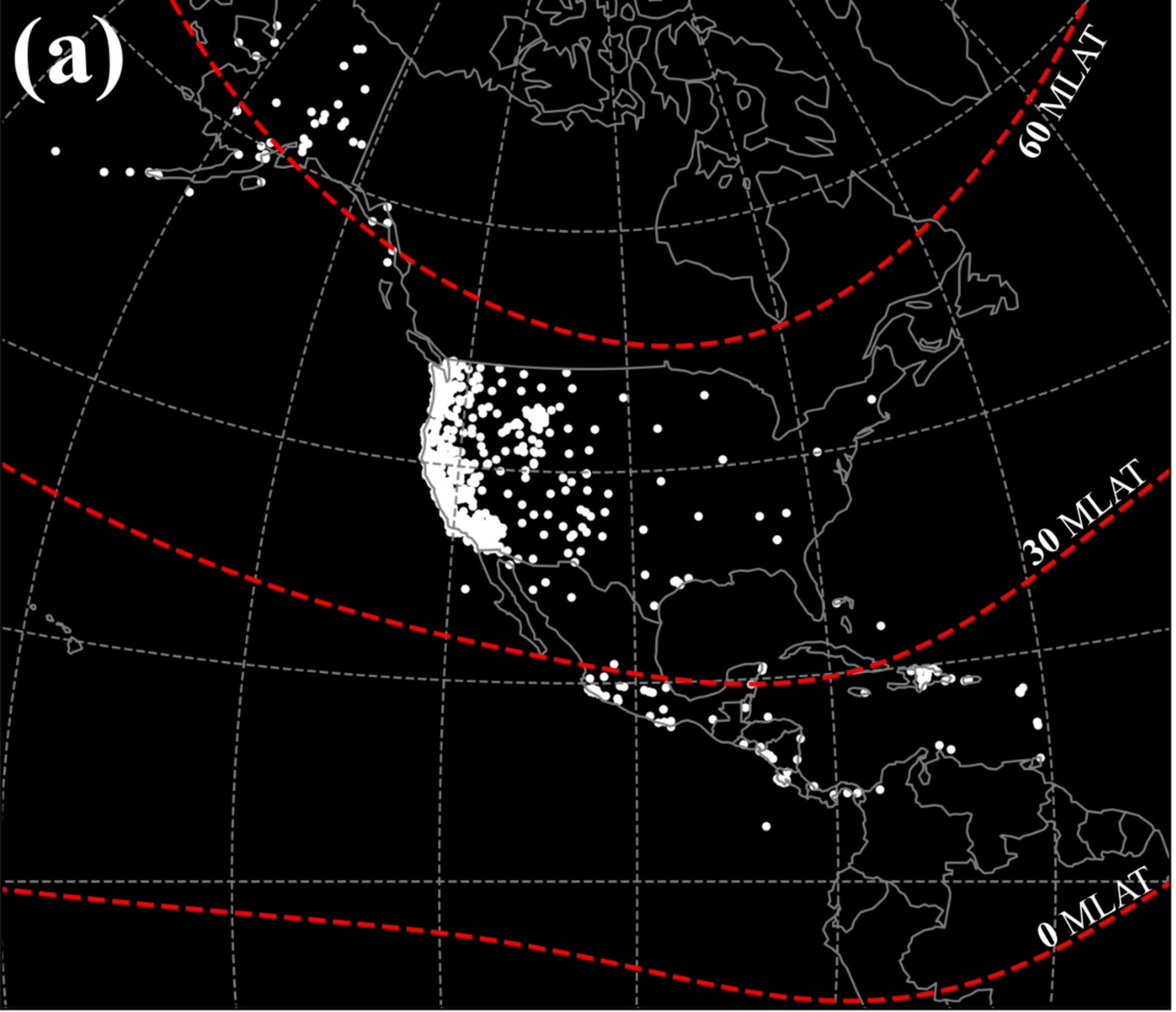
(a)
60 MLAT
30 MLAT
0 MLAT

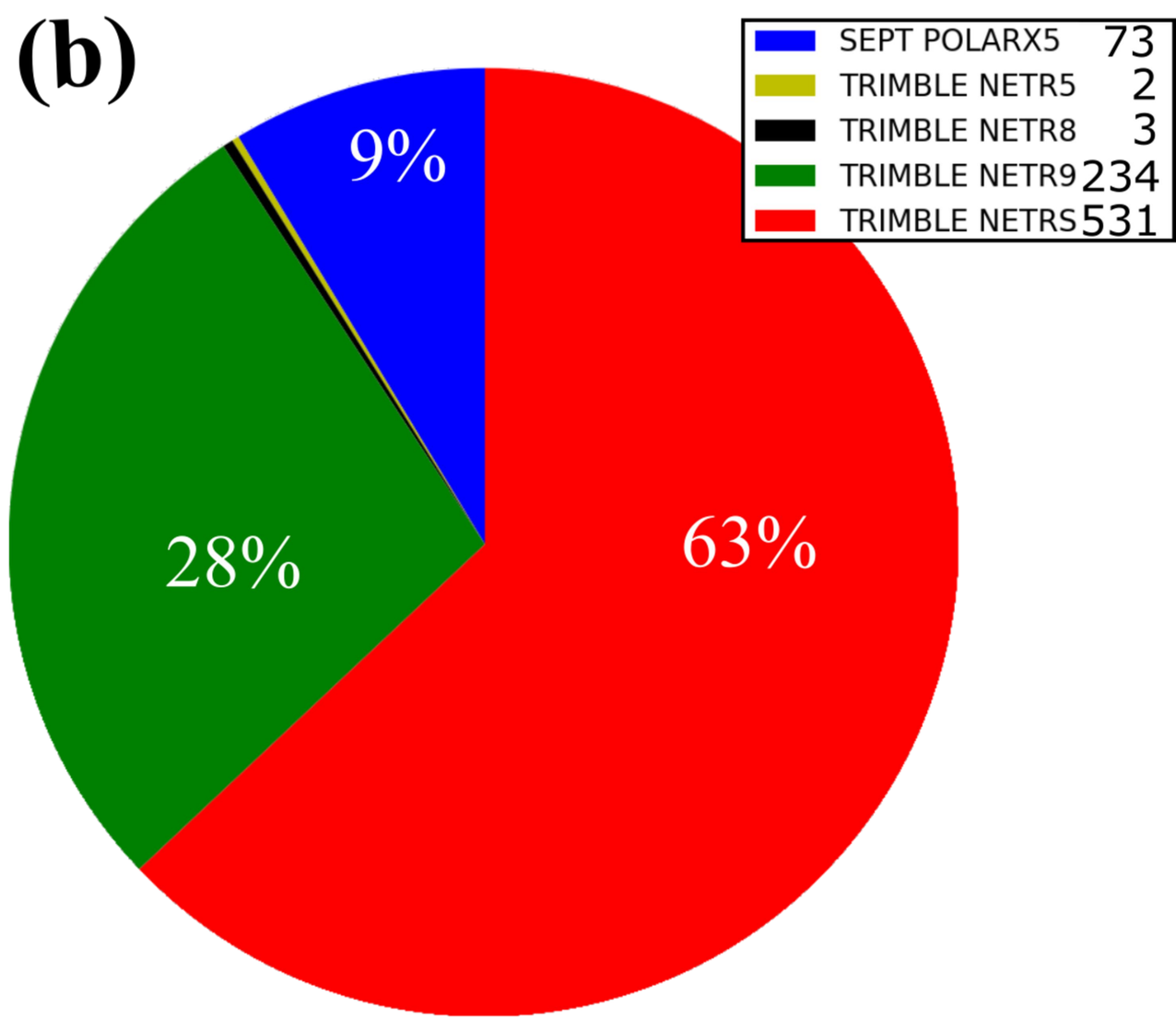
(b)
SEPT POLARX5 73
TRIMBLE NETR5 2
TRIMBLE NETR8 3
TRIMBLE NETR9 234
TRIMBLE NETRS 531
9%
28%
63%

Figure2.

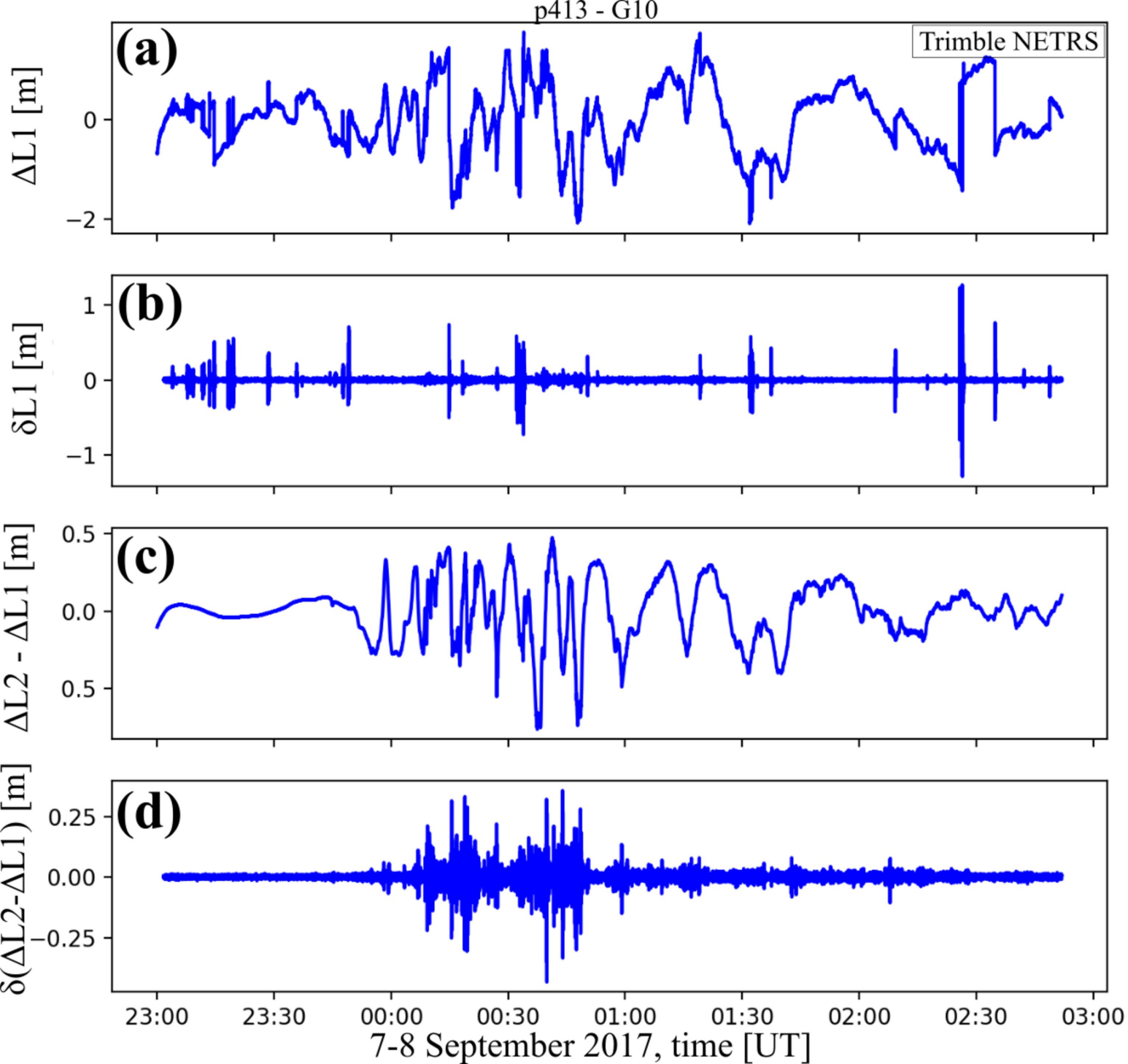
p413 - G10
(a)
Trimble NETRS
ΔL1 [m]
0
−2
(b)
δL1 [m]
1
0
−1
(c)
ΔL2 - ΔL1 [m]
0.5
0.0
0.5
(d)
δ(ΔL2-ΔL1) [m]
0.25
0.00
−0.25
23:00
23:30
00:00
00:30
01:00
01:30
02:00
02:30
03:00
7-8 September 2017, time [UT]

Figure3.

(a)

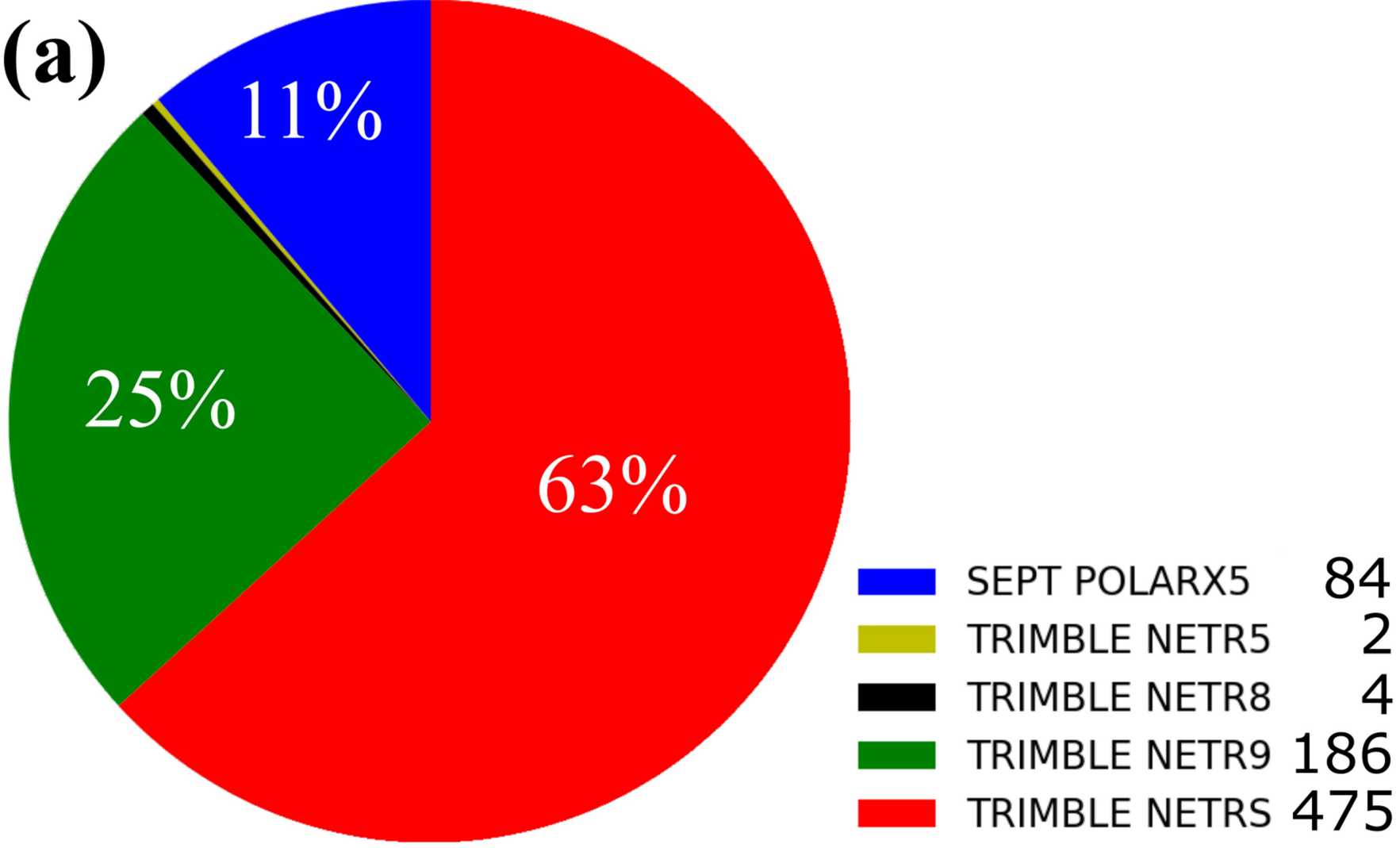
11%
25%
63%
SEPT POLARX5 84
TRIMBLE NETR5 2
TRIMBLE NETR8 4
TRIMBLE NETR9 186
TRIMBLE NETRS 475

(b)

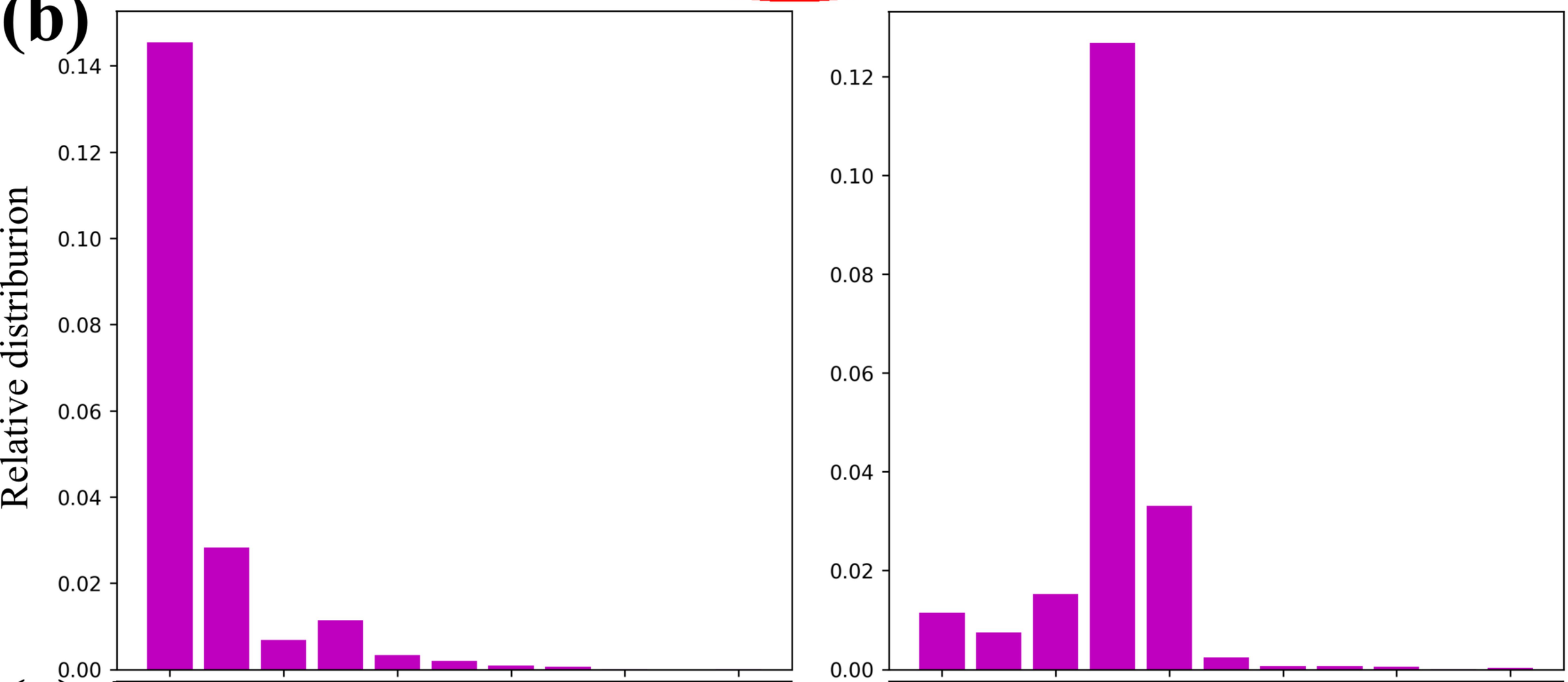
Relative distriburion
0.14
0.12
0.10
0.08
0.06
0.04
0.02
0.00
0.12
0.10
0.08
0.06
0.04
0.02
0.00

(c)

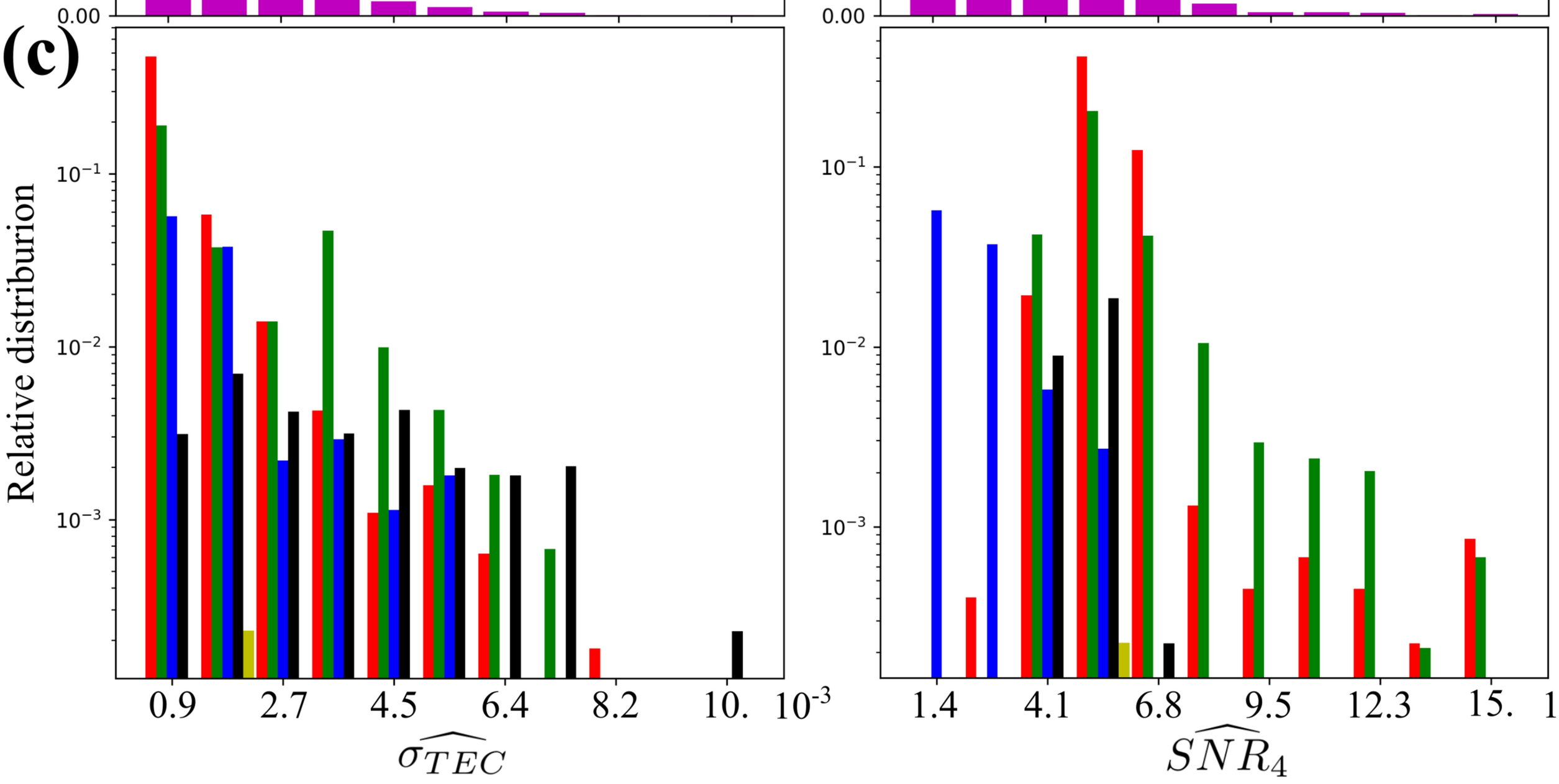
Relative distriburion
10^{-1}
10^{-2}
10^{-3}
0.9
2.7
4.5
6.4
8.2
10.
10^{-3}
$\widehat{\sigma_{TEC}}$
10^{-1}
10^{-2}
10^{-3}
1.4
4.1
6.8
9.5
12.3
15.
10^{-2}
$\widehat{SNR_4}$

Figure4.

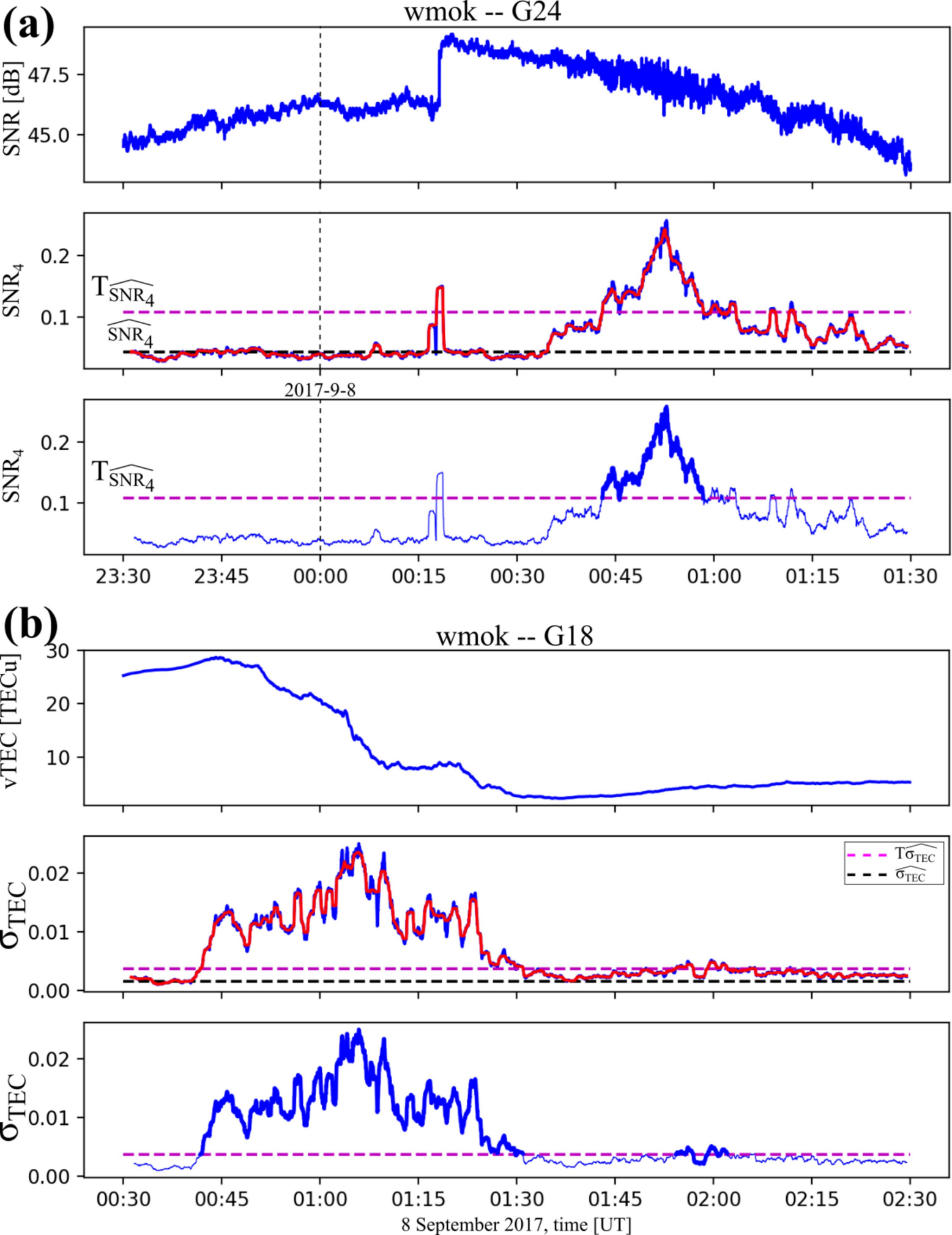
(a)
wmok -- G24
SNR [dB]
47.5
45.0
SNR4
0.2
0.1
T SNR4
SNR4
2017-9-8
SNR4
0.2
0.1
T SNR4
23:30
23:45
00:00
00:15
00:30
00:45
01:00
01:15
01:30
(b)
wmok -- G18
vTEC [TECu]
30
20
10
σTEC
0.02
0.01
0.00
Tσ TEC
σ TEC
σTEC
0.02
0.01
0.00
00:30
00:45
01:00
01:15
01:30
01:45
02:00
02:15
02:30
8 September 2017, time [UT]

Figure5.

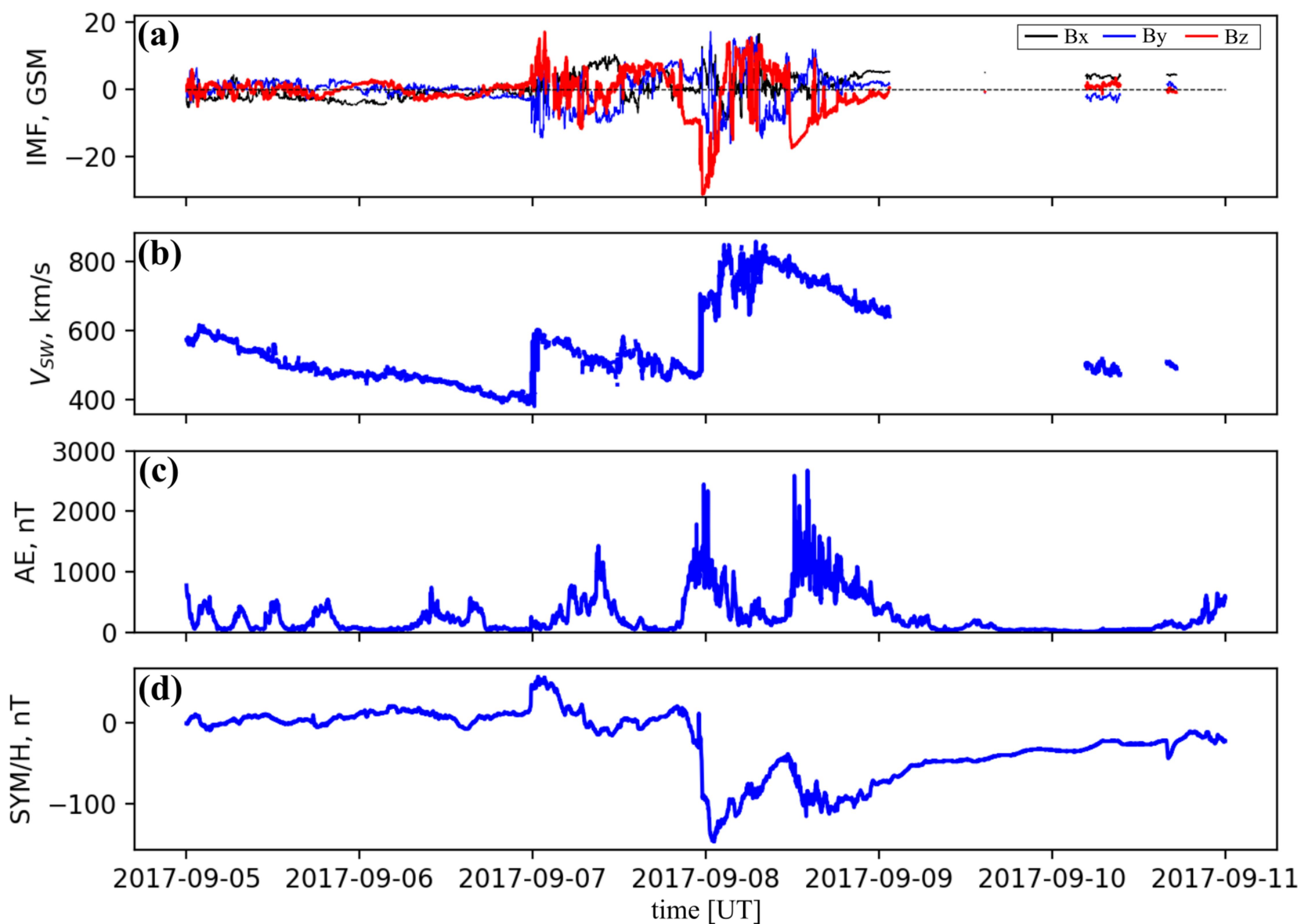
(a)
IMF, GSM
20
0
−20
Bx
By
Bz
(b)
V_{SW}, km/s
800
600
400
(c)
AE, nT
3000
2000
1000
0
(d)
SYM/H, nT
0
−100
2017-09-05
2017-09-06
2017-09-07
2017-09-08
2017-09-09
2017-09-10
2017-09-11
time [UT]

Figure6.

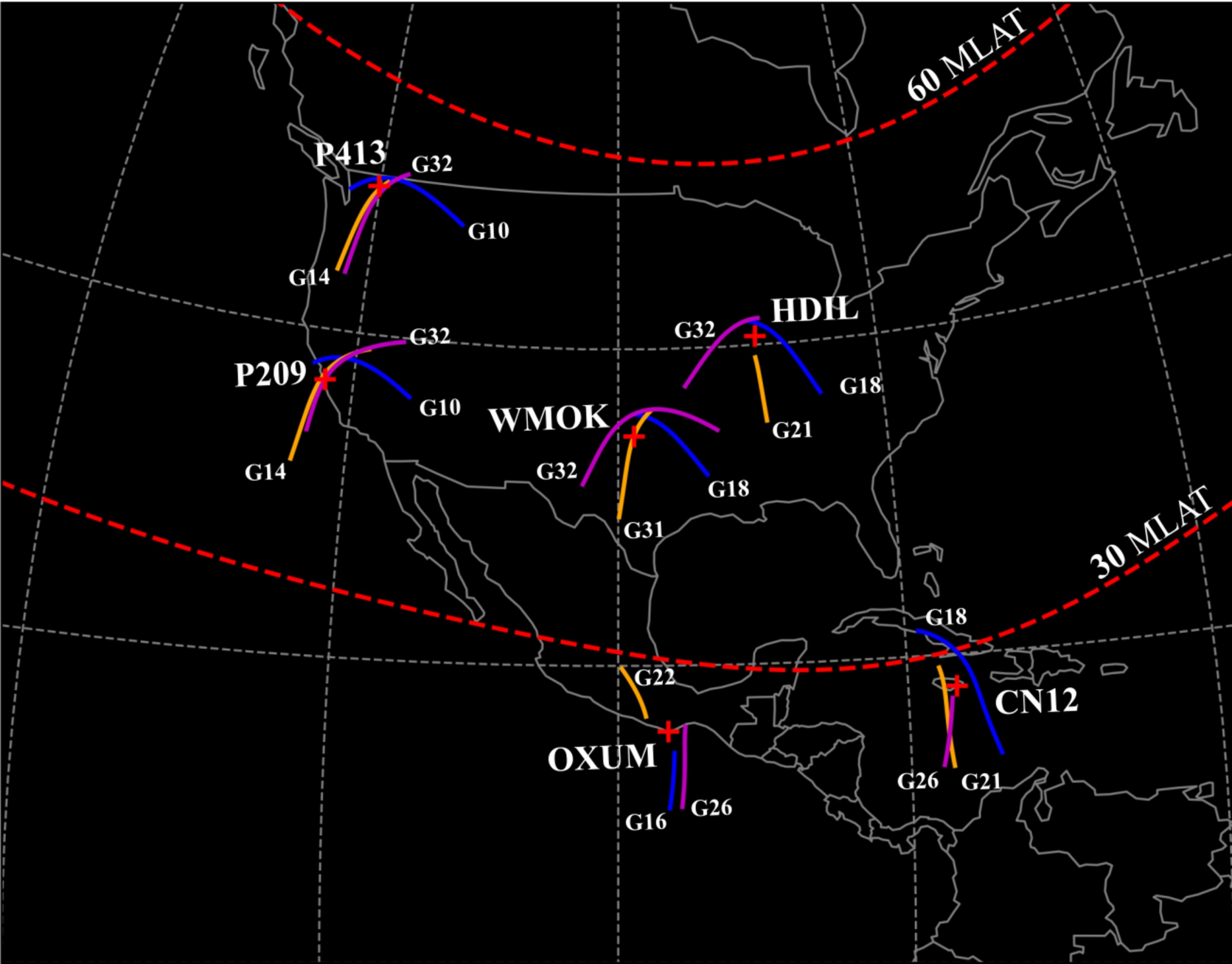
60 MLAT
30 MLAT
P413
G32
G10
G14
P209
G32
G10
G14
HDIL
G32
G18
G21
WMOK
G32
G18
G31
G18
G22
OXUM
G16
G26
CN12
G26
G21

Figure7.

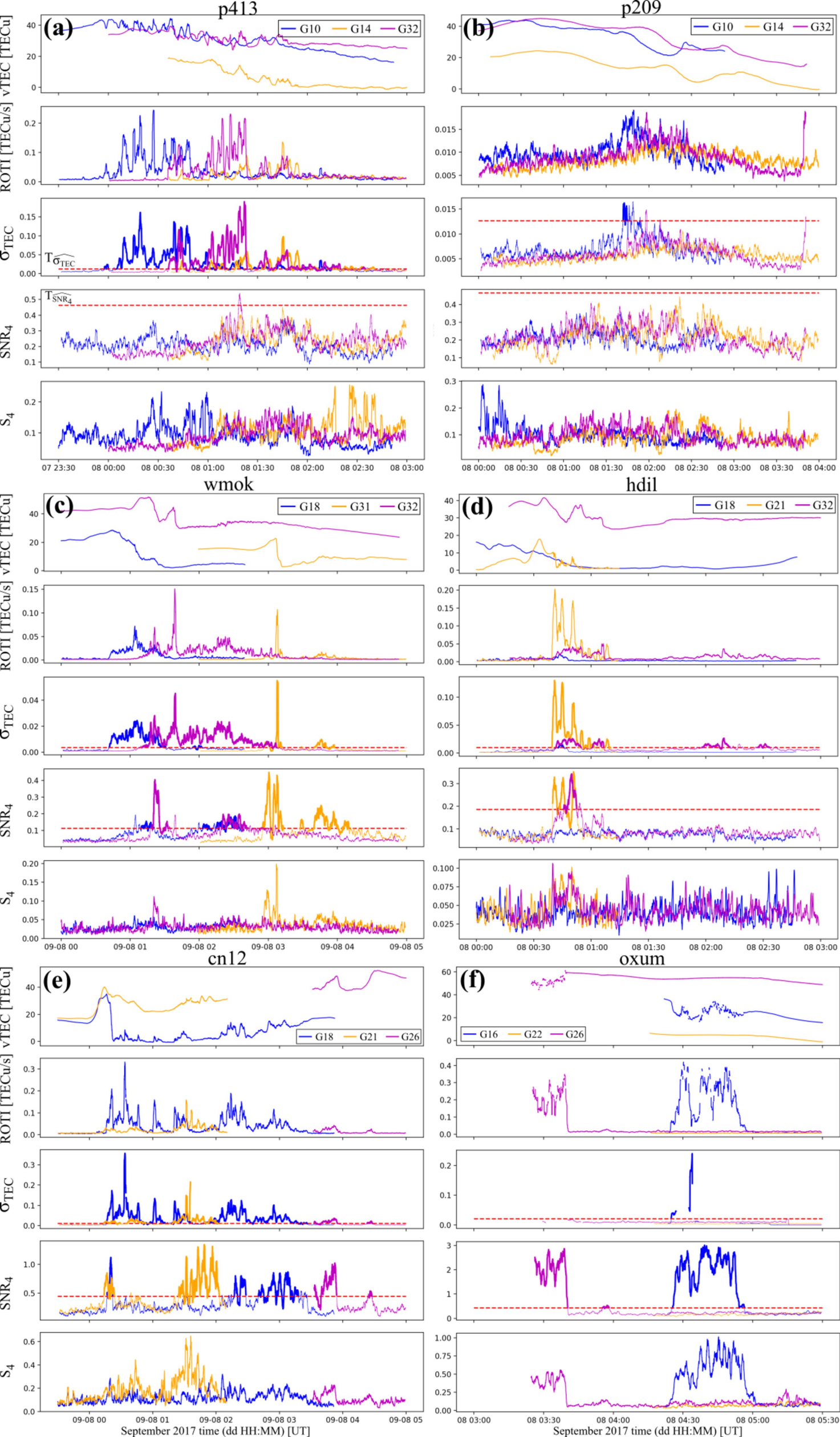
p413
p209
wmok
hdil
cn12
oxum
(a)
(b)
(c)
(d)
(e)
(f)
G10 G14 G32
G18 G31 G32
G18 G21 G32
G18 G21 G26
G16 G22 G26
vTEC [TECu]
ROTI [TECu/s]
σTEC
SNR4
S4
September 2017 time (dd HH:MM) [UT]

Figure8.

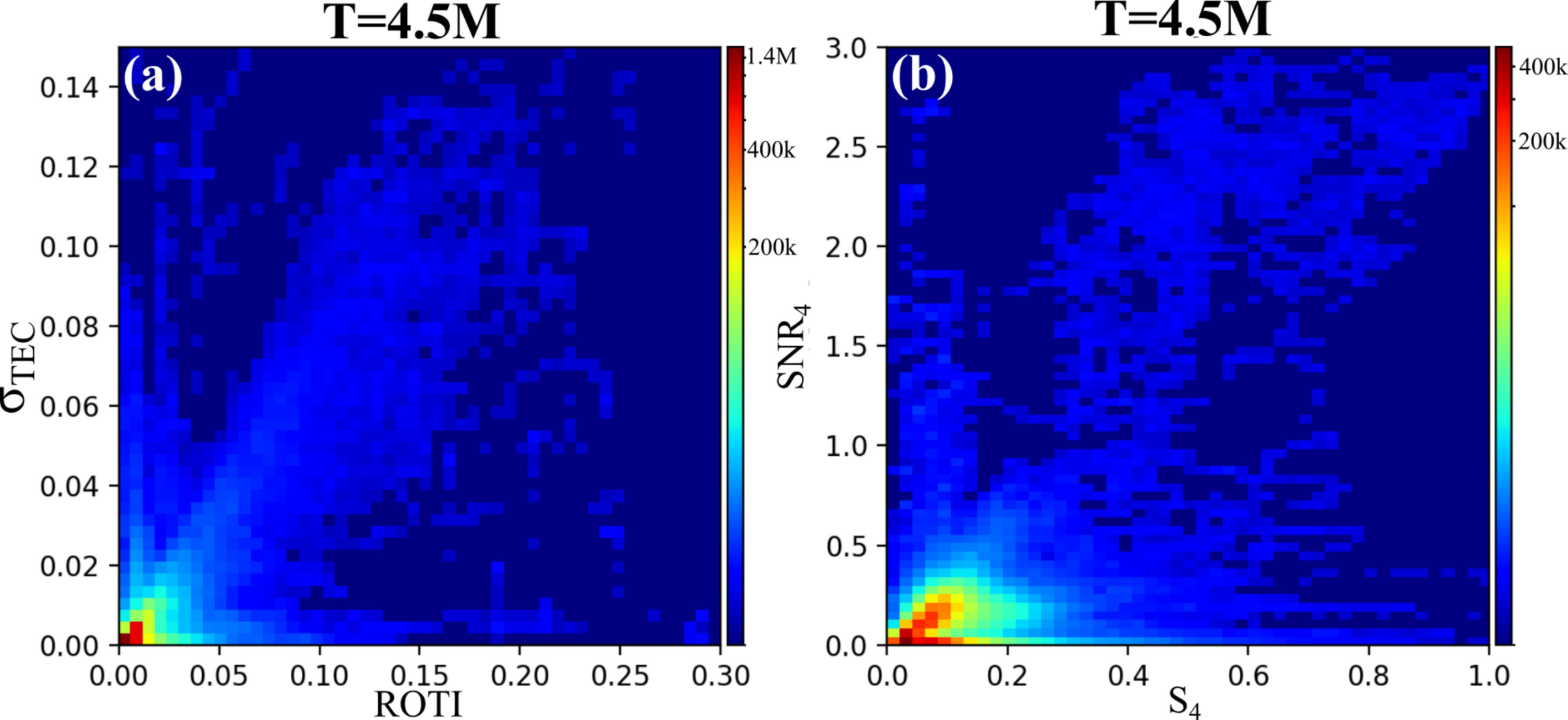
T=4.5M
(a)
1.4M
400k
200k
0.14
0.12
0.10
0.08
0.06
0.04
0.02
0.00
σTEC
0.00
0.05
0.10
0.15
0.20
0.25
0.30
ROTI
T=4.5M
(b)
400k
200k
3.0
2.5
2.0
1.5
1.0
0.5
0.0
SNR4
0.0
0.2
0.4
0.6
0.8
1.0
S4

Figure9.

(a)

T=196k

y=0.6x

R=0.93

σ_{TEC}

ROTI

T=49k

y=3.0x

R=0.882

SNR_4

S_4

(b)

T=7.1M

y=0.6x

R=0.902

σ_{TEC}

ROTI

T=745k

y=2.9x

R=0.83

SNR_4

S_4

Figure10.

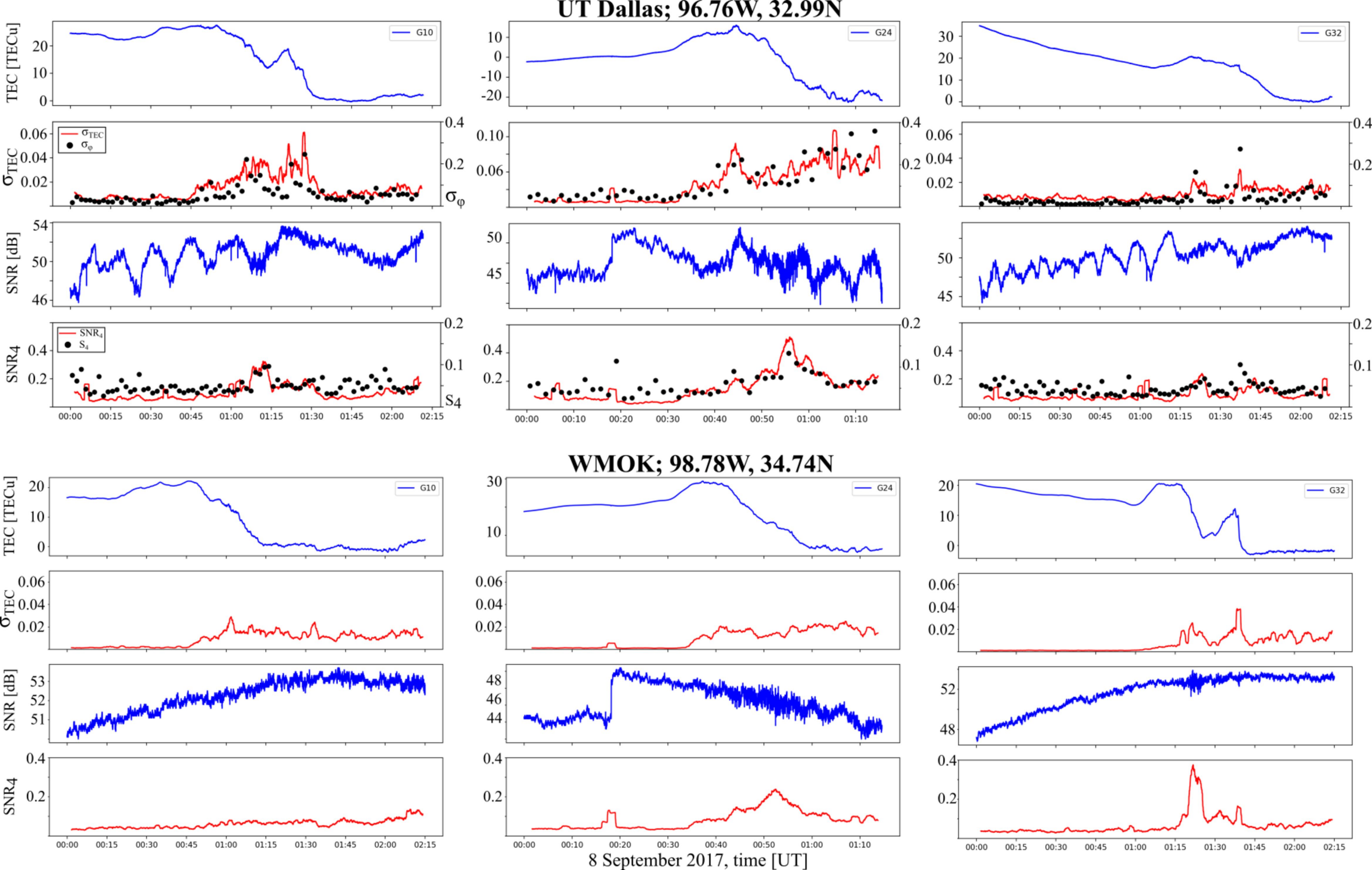
UT Dallas; 96.76W, 32.99N
WMOK; 98.78W, 34.74N
G10
G24
G32
TEC [TECu]
σTEC
σφ
SNR [dB]
SNR4
S4
8 September 2017, time [UT]

Figure11.

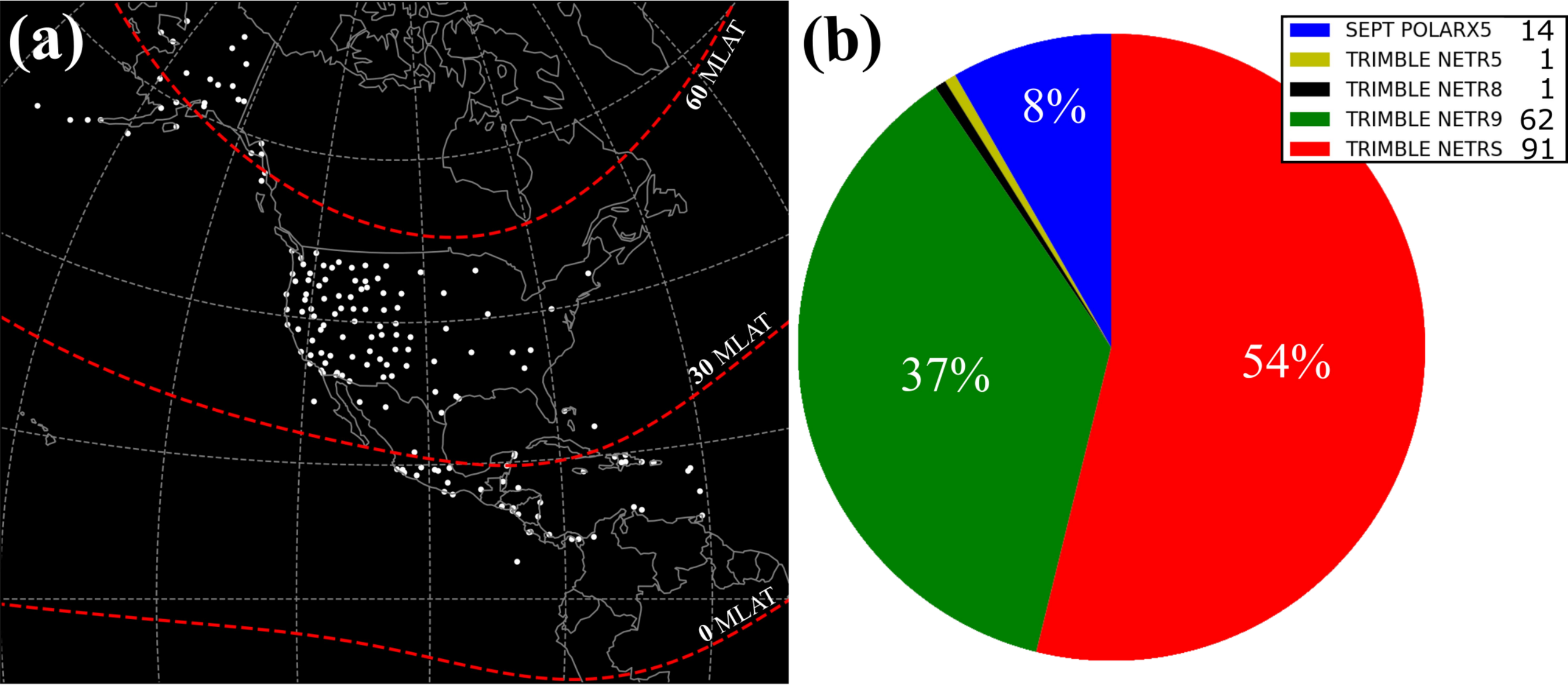
(a)
60 MLAT
30 MLAT
0 MLAT
(b)
SEPT POLARX5 14
TRIMBLE NETR5 1
TRIMBLE NETR8 1
TRIMBLE NETR9 62
TRIMBLE NETRS 91
8%
37%
54%

Figure12.

ROTI maps

Scintillation maps

(a) 09-07 23:30

(b) 09-08 00:30

(c) 09-08 01:30

40

20

0 mlat

-80

-40

0 mlon

09-07 23:30

09-08 00:30

09-08 01:30

mid-latitude trough

secondary trough

(d) 09-08 02:30

(e) 09-08 03:30

(f) 09-08 04:30

0. 0.01 0.02

ROTI [TECu/s]

09-08 02:30

09-08 03:30

09-08 04:30

0. 10 20

TEC [TECu]

0. 0.15 0.3

SNR_4

0. 0.04 0.08

σ_{TEC}

Figure13.

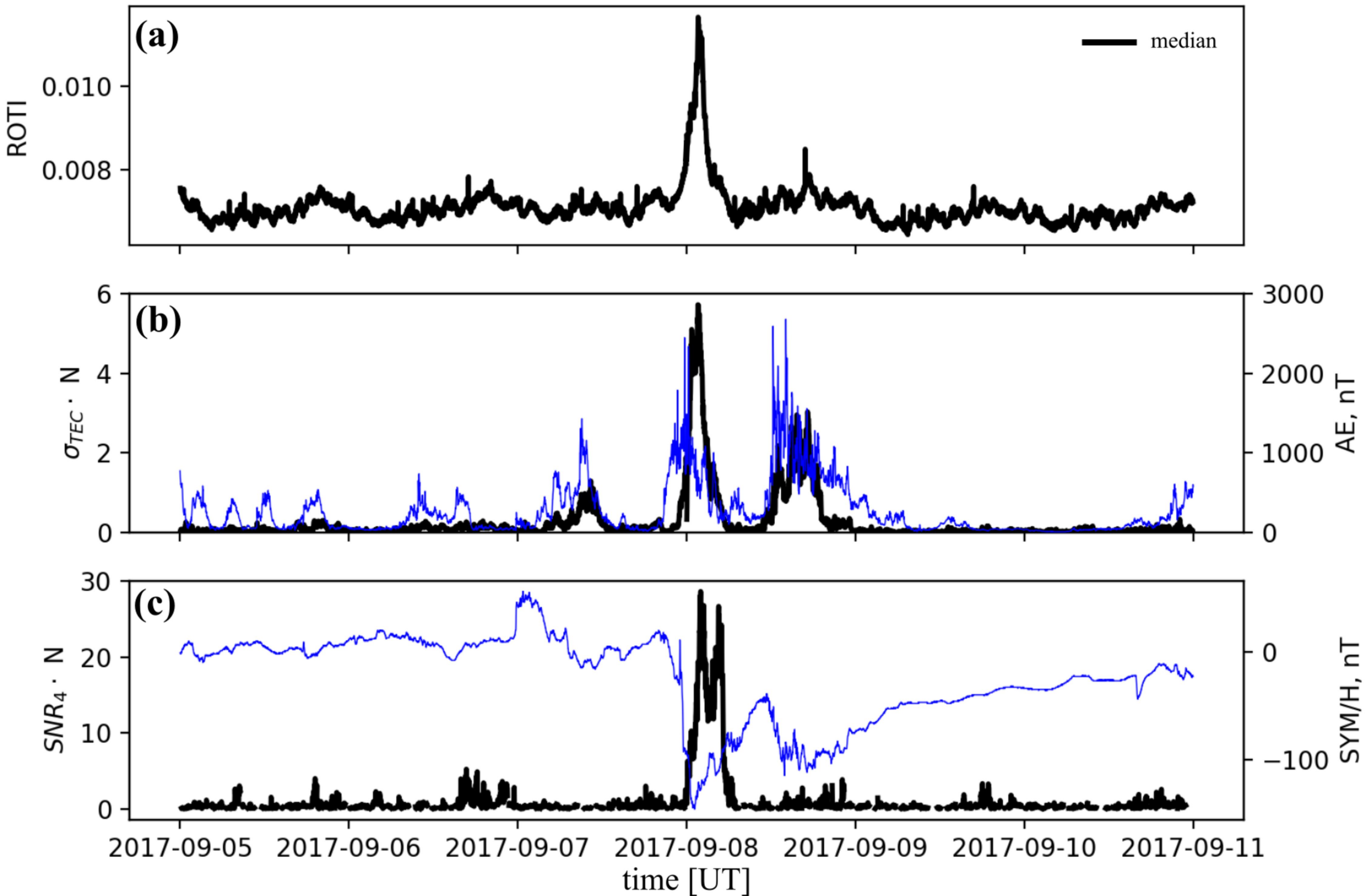
(a)
median
ROTI
0.010
0.008
(b)
σ_{TEC} · N
AE, nT
6
4
2
0
3000
2000
1000
0
(c)
SNR_4 · N
SYM/H, nT
30
20
10
0
0
−100
2017-09-05
2017-09-06
2017-09-07
2017-09-08
2017-09-09
2017-09-10
2017-09-11
time [UT]